UNIVERSIDADE FEDERAL DO RIO GRANDE DO SUL
INSTITUTO DE INFORMÁTICA
PROGRAMA DE PÓS-GRADUAÇÃO EM COMPUTAÇÃO

VITOR FERNANDO PAMPLONA

Photorealistic Models for Pupil Light Reflex and Iridal Pattern Deformation

Thesis presented in partial fulfillment
of the requirements for the degree of
Master of Computer Science

Prof. Dr. Manuel M Oliveira
Advisor

Prof. Dr. Gladimir V. G Baranoski
Coadvisor

Porto Alegre, April 2008

CIP – CATALOGING-IN-PUBLICATION

Pamplona, Vitor Fernando

Photorealistic Models for Pupil Light Reflex
and Iridal Pattern Deformation / Vitor Fernando Pamplona. – Porto Alegre: PPGC da UFRGS, 2008.

83 f.: il.

Thesis (Master) – Universidade Federal do Rio Grande do Sul. Programa de Pós-Graduação em Computação, Porto Alegre, BR–RS, 2008. Advisor: Manuel M Oliveira; Coadvisor: Gladimir V. G Baranoski.

1. Pupil-dynamics simulation. 2. Physiologically-based model. 3. Pupil light reflex. 4. Iridal pattern deformation. 5. Human visual system. 6. Face animation. I. Oliveira, Manuel M. II. Baranoski, Gladimir V. G. III. Title.

“Sete semanas? O Sr. é um fanfarrão, Sr. 01! O senhor tem sete dias, Sr. 01! ”
— CAPITÃO NASCIMENTO FACTS

ACKNOWLEDGMENTS

A special thanks goes to my advisors: Manuel Menezes de Oliveira Neto, who always help me to push my limits, teach me the “science-based way of life”, who helped me in the experiments and for the great improvements in all six papers submitted during this program; and Gladimir V. G. Baranoski for pushing me toward the use of bio-physical references, for suggesting the idea of exploring the iris and for the discussions along the period.

I am grateful for resources, contributions and suggestions from Prof. Jacobo Melamed Cattan (Ophthalmology-UFRGS), who helped me dilating the pupils of several volunteers and let me use the colored videos from the Keratometer; and Prof. Luis A. V. Carvalho (USP-SC) for the videos of an infrared Keratometer.

Thanks to Leandro A. F. Fernandes, Marcos Slomp, Eduardo Gastal and Denison L. M. Tavares who contributed in the demos and videos for papers based on this work. Leandro Lichtenfelz (Mathematics-UFSC), Renato Silveira and Prof. Roberto da Silva, for the help with advanced mathematical concepts and discussions. Ida Rossi (Librarian-UFRGS) for finding a lot of very old biological papers, Fernando Trebien and André Spritzer for english revisions, and Cinara Cunha (Arts-FURB) for give me permission to use her iris photo as a motivation of this work. I also thank the volunteers of the experiments: Alex Gimenes, Boris P. Starov, Christian Pagot, Claudio L. Menezes, Giovane R. Kuhn, Leonardo Schmitz, Rodrigo Mendes, Tiago Etiene and specially João Paulo Gois who receive me at USP/São Carlos.

I would like to thank the professors Carla M.D.S. Freitas, João D. Comba, Luciana P. Nedel and Manuel M. Oliveira for conducting the UFRGS Computer Graphics Group to a level of excellence and to my lab colleagues for providing an intellectually stimulating and enjoyable research environment. Fausto Blanco and Francisco de Moura Pinto for discussions about the academic and commercial ways of life, and Fabio Bernardon for always saying that there is no practical utility in my work, holding my ego in a normal stage. To my family and all my friends, especially my parents Marli Knuth Pamplona and Carlos Fernando Pamplona (in memoriam), my brother Paulo Roberto Pamplona for tolerating my absence of their lives.

Thanks to Microsoft Brazil for the financial support during the seven final months. Thanks to Prof. Paulo C. Rodacki (FURB) and Jomi Fred Hubner (FURB) for the recommendation letters and to Prof. Anatolio Laschuk to be ready when I needed help to record some videos at Hospital de Clínicas (University Hospital).

I also thanks the people that take part of our soccer games and lab parties, my neighbor Márcia M. Moraes and her family, and the cookies woman, Eliane, for giving me instants of a normal life even into a Master’s program.

TABLE OF CONTENTS

LIST OF FIGURES

ABSTRACT

This thesis introduces a physiologically-based model for pupil light reflex (PLR) and an image-based model for iridal pattern deformation. The PLR model expresses the pupil diameter as a function of the environment lighting, naturally adapting the pupil diameter even to abrupt changes in light conditions. Since the parameters of the PLR model were derived from measured data, it correctly simulates the actual behavior of the human pupil. The model is extended to include latency, constriction and dilation velocities, individual differences and some constrained random noise to model hippus. The predictability and quality of the simulations were validated through comparisons of modeled results against measured data derived from experiments also described in this work.

Another contribution is a model for realist deformation of the iris pattern as a function of pupil dilation and constriction. The salient features of the iris are tracked in photographs, taken from several volunteers during an induced pupil-dilation process, and an average behavior of the iridal features is defined. The effectiveness and quality of the results are demonstrated by comparing the renderings produced by the models with photographs and videos captured from real irises.

The resulting models produce high-fidelity appearance effects and can be used to produce real-time predictive animations of the pupil and iris under variable lighting conditions. Combined, the proposed models can bring facial animation to new photorealistic standards.

Keywords: Pupil-dynamics simulation, Physiologically-based model, Pupil light reflex, Iridal pattern deformation, Human visual system, Face animation.

Modelos Fotorealistas para Dinâmica Pupilar em Função da Iluminação e Deformação dos Padrões da Íris

RESUMO

Este trabalho introduz um modelo fisiológico para o reflexo pupilar em função das condições de iluminação (*Pupil Light Reflex* - PLR), e um modelo baseado em imagem para deformação dos padrões da íris. O modelo para PLR expressa o diâmetro da pupila ao longo do tempo e em função da iluminação ambiental, sendo descrito por uma equação diferencial com atraso, adaptando naturalmente o tamanho da pupila a mudanças bruscas de iluminação. Como os parâmetros do nosso modelo são derivados a partir de modelos baseados em experimentos científicos, ele simula corretamente o comportamento da pupila humana para um indivíduo médio. O modelo é então estendido para dar suporte a diferenças individuais e a hippus, além de utilizar modelos para latência e velocidade de dilatação e contração.

Outra contribuição deste trabalho é um modelo para deformação realista dos padrões da íris em função da contração e dilatação da pupila. Após capturar várias imagens de íris de diversos voluntários durante diferentes estágios de dilatação, as trajetórias das estruturas das íris foram mapeadas e foi identificado um comportamento médio para as mesmas. Demonstramos a eficácia e qualidade dos resultados obtidos, comparando-os com fotografias e vídeos capturados de íris reais. Os modelos aqui apresentados produzem efeitos foto-realistas e podem ser utilizados para produzir animações preditivas da pupila e da íris em tempo real, na presença de variações na iluminação. Combinados, os dois modelos permitem elevar a qualidade de animações faciais, mais especificamente, animações da íris humana.

Palavras-chave: Simulação de dinâmica pupilar, modelo fisiológico, reflexo pupilar a luz, deformação de padrões da íris, sistema visual humano, animação facial.

1 INTRODUCTION

Arguably, the most important feature in facial animation are the eyes, which are essential not only in directing the gaze of the audience (LEE; BADLER; BADLER, 2002), but also in conveying the appropriate degree of expression through pupil dilation and constriction movements (WATT; WATT, 1992). Hence, for animations depicting close-up views of the face (Figure 1.1), natural-looking eyes and pupil movements are highly desirable.

> Walt Disney once said to his animation team that the audience watches the eyes and this is where the time and money must be spent if the character is to act convincingly (WATT; WATT, 1992).

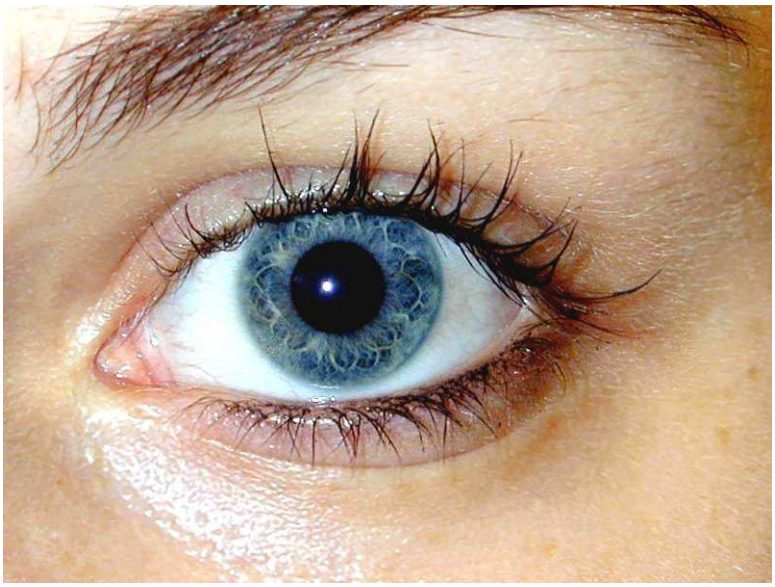

Figure 1.1: Photograph of a human iris. Image courtesy of Cinara Cunha.

Differently from most of the body, the human eye is subject to some involuntary movements of the pupil, which are determined by ambient illumination, focal length, drug action, and emotional conditions, among others (REEVES, 1920; ELLIS, 1981; CALCAGNINI et al., 2000). Pupillary light reflex (PLR) is responsible for the constriction of the pupil area in highly lit environments and for its dilation in dimmed ones. Spontaneous irregular variations in pupil diameter are called hippus, occurring in a frequency range of 0.05 to 0.3Hz, oriented by the nervous system (TREVOR-ROPER; CURRAN, 1984; STARK, 1939). PLR and hippus are an integral part of our daily experience and, except for drug-induced action, is the most noticeable of such involuntary movements of

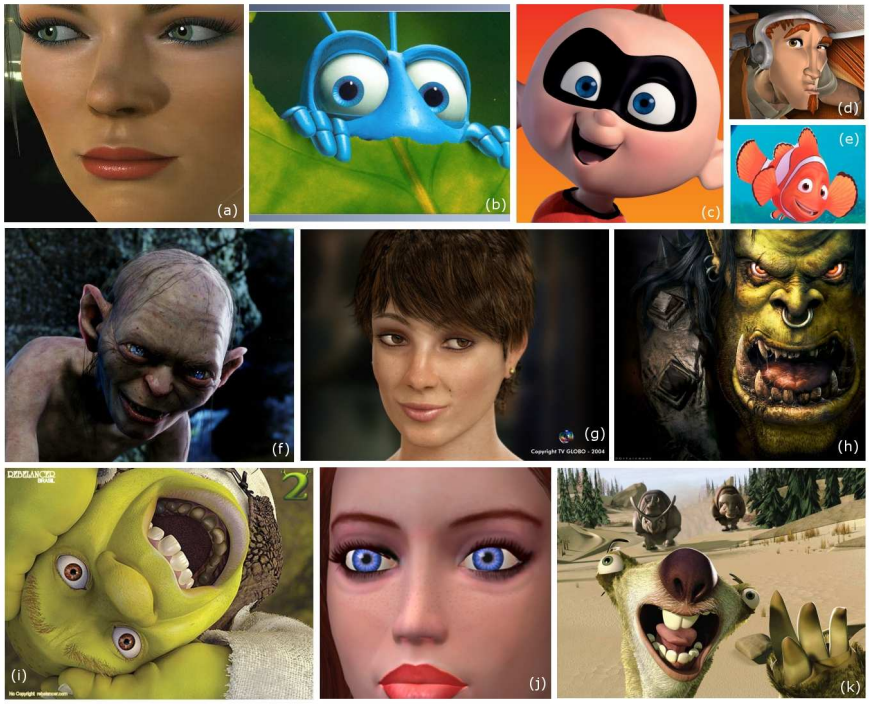

Figure 1.2: Examples of close up scene in recent movies/animations: (a) Nvidia's model, Adrianne (nVidia nZone, 2007); (b) Flik in Bug's Life (SfondiDelDesktop.com, 2007); (c) Jack-Jack in The Incredibles (PIXAR, 2007a); (d) Monkey from Acceleracers (HOT WHEELS, 2007); (e) Marlin from Finding Nemo (PIXAR, 2007b); (f) Gollum from Lord of the rings (MMVII New Line Productions, 2004); (g) Eva Byte, presenter of Fantástico at TV Globo (GLOBO, 2004); (h) Orc from Warcraft game (ESCALOFRIO.FREE.FR, 2007); (i) Shrek in Shrek 2 (REBELANCER, 2007); (j) Face from a simple blender tutorial (JCH DIGITAL DESIGNS, 2007); (k) Sid from Ice Age (TWENTIETH CENTURY FOX, 2006).

the pupil. As track of these the pupil movements by motion capture systems is impracticable, since the light conditions have to be simulated during the capture, this work creates a predictive biophysically-based approach to pupil movements.

The human iris, in its turn, is a muscular tissue containing several easily identifiable structures, such as the collarette, pigment spots, and crypts (Figure 1.1). Together, they define patterns, believed to be unique to each person (DAUGMAN, 2002), that are deformed as a result of changes in the pupil diameter. Although pupil light reflex and iridal deformations could be animated using standard computer graphics techniques, such as parametric representations controlled by velocity curves (WATT; WATT, 1992), the use of physiologically-based models guided by physically meaningful parameters can make the process more predictable and automatic, which, in turn, may result in more realistic and reproducible animations of these movements.

This thesis presents a physiologically-based model for realistic animation of pupil dynamics and iridal pattern deformation. The model combines some theoretical results from the field of Mathematical Biology (LONGTIN; MILTON, 1989) with experimental data collected by several researchers relating pupil diameter to the intensity of environmental light (MOON; SPENCER, 1944). The proposed model is extended to support individual differences, hippus simulation and latency and velocity models. The iridal pattern deformation is modeled by acquiring a set of high-resolution photographs of real irises

at different levels of pupillary dilation and by tracking their features across the set of images. By analyzing the tracked positions, a simple analytical expression for the iridal pattern deformation as a function of the pupil diameter is obtained (Section 6). The resulting model produces high-fidelity appearance effects and can be used to produce real-time predictive animations of the pupil and iris under variable lighting conditions (Section 5.5). To the best of our knowledge, these models are the first physiologically-based model for simulating pupil light reflex presented in the graphics literature (the first model ever to simulate individual variability in terms of PLR sensitivity - Section 5.4), as well as the first model for iridal pattern deformation. The effectiveness and quality of the models are demonstrated by comparing the results with photographs and videos taken from real irises (Figure 1.3). Table 1 summarizes the main mathematical and physical quantities considered throughout this work.

Symbol	Description	Physical Unit
t	current simulation time	milliseconds (ms)
τ	pupil latency	milliseconds (ms)
L_{fL}	luminance	foot-Lambert (fL)
L_b	luminance	blondels (B)
I	illuminance	lumens/mm^2 or lux
R	light frequency	hertz (Hz)
D	pupil diameter	millimeter (mm)
A	pupil area	squared millimeter (mm^2)
β, α, γ, k	rate constant	none
ϕ	retinal light flux	lumens (lm)
$\bar{\phi}$	retinal light flux threshold	lumens (lm)
x	muscular activity	none
r_I	individual variation (iso-curve)	$r_I \in [0, 1]$

Table 1.1: Table of symbols. A summary of the the main mathematical and physical quantities considered in the development of the proposed models.

1.1 Structure of this Thesis

The remaining of this thesis is organized as follow: Chapter 2 discusses some techniques for image synthesis of the human iris and eye. Chapter 3 reviews the eye anatomy and physiology and presents a mathematical model for iris structure. Chapter 4 presents models for pupillary movements, latency and constriction/dilation velocity. Chapter 5 introduces the model for pupil light reflex and extends it to simulate hippus and individual differences. Chapter 6 presents the image-based model for iridal pattern deformation. Chapter 7 discusses an application example in computer graphics showing a human face rendered using the proposed models to simulate the pupil and iris responses to the environmental light. Finally, Chapter 8 summarizes this thesis and lists some avenues for future exploration.

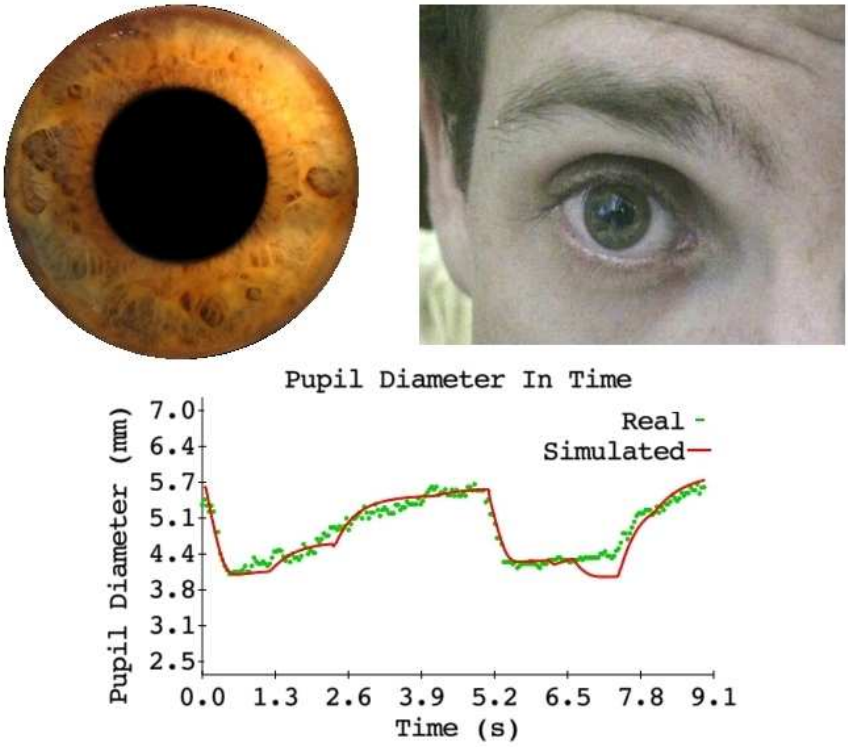

Figure 1.3: The comparison of the proposed models with real irises: (Top-Left) the results of the proposed pupil light reflex and iridal pattern deformation models; (Top-Right) A frame from a nine-second-long video sequence showing a human iris exposed changes in lighting conditions; (Bottom) a graph comparing the pupil diameter as a function of time. The dots represent the values manually measured for each frame of the video sequence. The solid line shows the simulated results obtained with the PLR model. Note how the simulated results satisfactorily predict the real ones.

2 RELATED WORK IN COMPUTER GRAPHICS

A few researchers have addressed the issue of realistic human iris synthesis. Lefohn *et al.* (2003), based on ocularist knowledge, created a model for the human iris blending[1] several layers of semi-transparent textures, each one containing some eye feature, mapped in cones (Figure 2.1). The textures are created by artists and carry no information about the physiology of the iris.

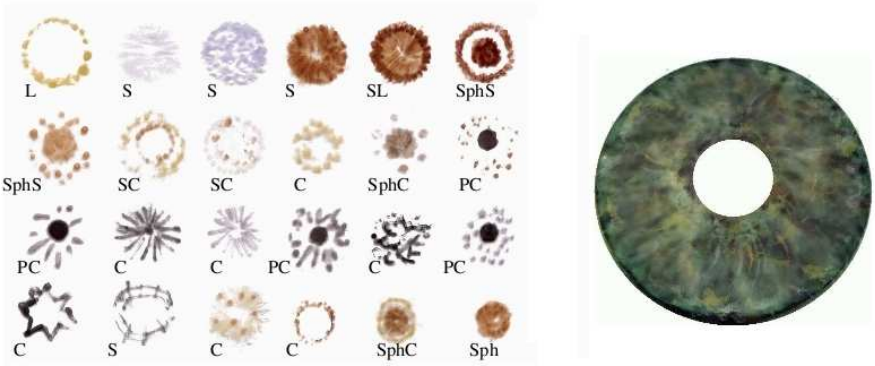

Figure 2.1: Results from Lephon *et al.*: (left) Example textures containing Stroma (S), collarette (C), limbus (L), pupil (P) and sphincter muscle (Sph) components; (right) The final synthetic iris. From (LEFOHN et al., 2003)

Other image-based approaches have been proposed by Cui *et al.* (2004), Wecker *et al.* (2005) and Makthal and Ross (2005). Essentially, they decompose a set of iris images using techniques such as principal component analysis[2] (CUI et al., 2004), multi-resolution and wavelets[3] (WECKER; SAMAVATI; GAVRILOVA, 2005) and Markov random fields[4] (MAKTHAL; ROSS, 2005), and recombine the decomposed data to generate new images of irises. The algorithm proposed by Wecker *et al.*. needs a pre-processing stage where the center of the pupil and the iris are aligned and the pupil is removed. The algorithm can only join images with equal features (*i.e.* the number of high-frequency rings that were created by folds). The algorithm from Makthal and Ross mix two or more

[1] A weighted sum, pixel-by-pixel, over two or more semi-transparent images.

[2] A transformation where the data set receives a new coordinate system, in which new axes follow the directions of largest variances in the data set (CUI et al., 2004).

[3] A set of orthonormal basis functions used to decompose a given function (or continuous-time signal) into different frequency components. (WECKER; SAMAVATI; GAVRILOVA, 2005).

[4] Models used to describe the probability distribution governing the intensity values of pixels in a specific neighborhood (MAKTHAL; ROSS, 2005).

user-defined iris features cutted from iris images. It needs an user interaction to stop the iterator when a good iris image is rendered (Figure 2.2).

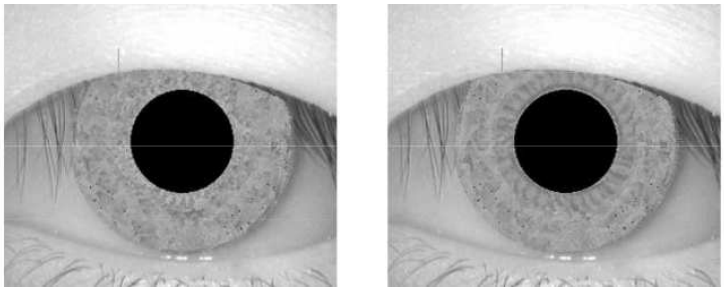

Figure 2.2: Two synthesized iris by Makthal and Ross method. From (MAKTHAL; ROSS, 2005)

Zuo and Schmid (2006; 2006) created a 3D model of the iris fibers. Each fiber is a continuous 3D curve in cylindrical coordinates, which is rendered using the conventional graphics pipeline (Figure 2.3). A final Gaussian-blur step is applied to the resulting image, which is then used to represent the iris.

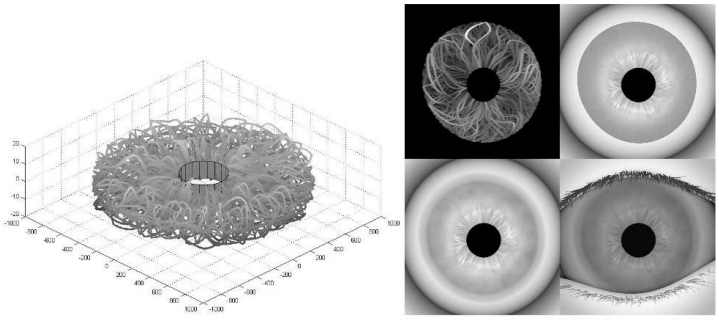

Figure 2.3: Results from Zuo and Schmid: (left) The 3D model for the collagen fibers and (right) the four steps of the algorithm: (i) projection of the fiber in image space; (ii) adding a semitransparent top layer with an irregular edge to simulate the collarette; (iii) blurring the root of the iris and add a noise layer; (iv) adding eyelids and eyelashes to the final synthetic iris. From (ZUO; SCHMID, 2006)

Lam and Baranoski (2006) introduced a predictive iridal light transport model (ILIT), which computes the spectral responses of iridal tissues described by biophysical parameters. As the result, their model predicts a uniform color to the iris using subsurface scattering techniques[5]. This model, however, does not address issues related to the morphology and dynamics of the iridal tissues.

Finally, François *et al.* (2008; 2007) estimate iris height maps[6] from gray-scale images. Since they assume the light scatters more in thicker regions of the iris and less in thinner parts, given a gray-scale picture of an iris, the darker parts of the image represent

[5]A set of simulation techniques in which the light penetrates the surface of a translucent material and is scattered by interacting with internal tissues of the object.

[6]An image where each pixel stores a height value. When associated to an object, the rendering process will add the height value to the 3D position in the object surface associated to that pixel. In graphics applications, a height map is used to simulate the displacement of a given surface according to the values stored in the map.

thinner structures of the iris and lighter parts, the ticker ones. The height map rendering allows, in close up views, the perception of shadows (Figure 2.4). Their future work intent to recover, from iris images, an approximation to respective densities of eumelanin and pheomelanin pigment found in Stromal and ABL layers (discussed in Chapter 3), needed by Lam and Baranoski model (2006).

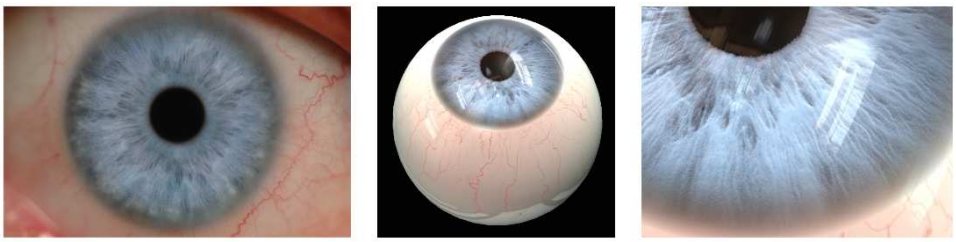

Figure 2.4: Results from François *et al.*: (left) Eye picture captured with polarizing filters to avoid corneal reflections; (middle) Rendering of the resulting iris model using the estimated height field; (right) Close up showing shadows. Images from (FRANÇOIS et al., 2008).

Sagar et al. (1994) developed an anatomically detailed model of the eye to be used in a surgical simulator. In their model, Gaussian perturbations were used to simulate the waviness of ciliary fibers and the retraction of pupillary fibers during pupil dilation. Alternatively, depending of the level of object manipulation, a texture mapping[7] approach was used to model the iridal appearance. It is worth noting, however, that their goal was to achieve functional realism (FERWERDA, 2003) as opposed to physical or photorealism.

All these models and techniques, however, do not handle pupillary movements nor deformation of iridal patterns.

[7] A technique for adding details, color or texture to the surfaces of geometric models used in graphics applications. Such details are stored on structures called "texture maps".

3 AN OVERVIEW OF THE HUMAN IRIS AND PUPIL

This chapter presents an overview of the human eye and the iris anatomy and physiology. Its goal is to familiarize the reader with terminology and some biological properties that will be relevant in the following chapters.

The eyes are a fundamental part of the visual system found in many organisms. They can vary from the simplest eye which only detects light or dark to the complex ones with 350 degrees of field of view. The eye translates electromagnetic radiation (light), from different wavelengths and intensities, to neural action potentials and sends them to the brain. Figure 3.1 shows the anatomy of the human eye.

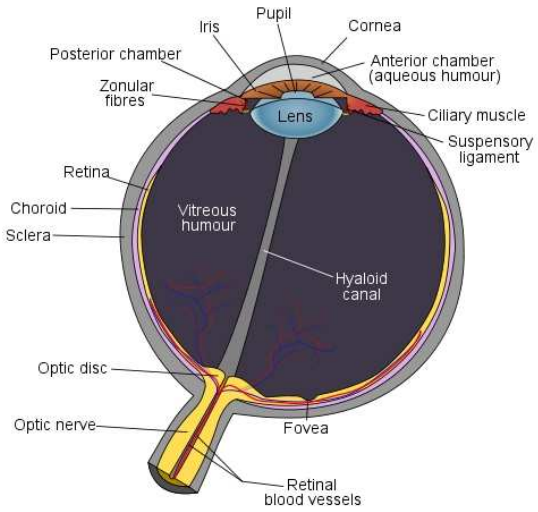

Figure 3.1: A sketch of the human eye internal structures. Source (WIKIPEDIA: the free encyclopedia, 2007).

In humans, the electromagnetic radiation enters in the eye by the cornea, an elliptic transparent layer with a refractive power of 43 diopters[1], roughly two-thirds of the eye's total refractive power (PROENÇA, 2006; BORES, 2002; BERG; TAN, 1994). The cornea is connected to the sclera, the white part of the eye. It contains collagen fibrils and elastin, just like the sclera, but has also a protein called keratin, that makes it transparent. Cornea and sclera protects other internal structures of the eye (BORES, 2002).

[1]The diopter is the optical power measurement unit which is equal to the reciprocal of the focal length measured in metres. For example, if a person has -4 diopters of nearsightedness, it means that the farthest point he/she can see clearly is one-fourth of a meter (about 10 inches) from his/her eye.

Behind the cornea, there is a thick watery substance called aqueous humour, constantly produced by the ciliary process inside the ciliary body and drained by the trabecular meshwork (Figure 3.2). It is responsible for providing nutrients to the lens and cornea (BORES, 2002). The aqueous humour let pass wavelengths from 220 nm and 2400 nm, however after 980 nm the light rays are gradually absorbed. This process is independent of age (BOETTNER; WOLTER, 1962).

The lens (also called crystalline lens) are a transparent, biconvex and flexible (lentil-shaped) structure with 15 diopters. It has from 7 to 9 mm of diameter and from 2 to 4.5 mm of depth (SCHACHAR, 2005). Its curvature and thickness are changed by the ciliary muscle to adjust the focal distance during the accommodation. The lens are affected by the age and the ratio of direct light transmission decreases along time (*i.e.* while a baby perceives wavelengths starting at 300 nm, an adult can only perceive wavelengths starting at 400nm on average) (BOETTNER; WOLTER, 1962; SCHMID et al., 2004).

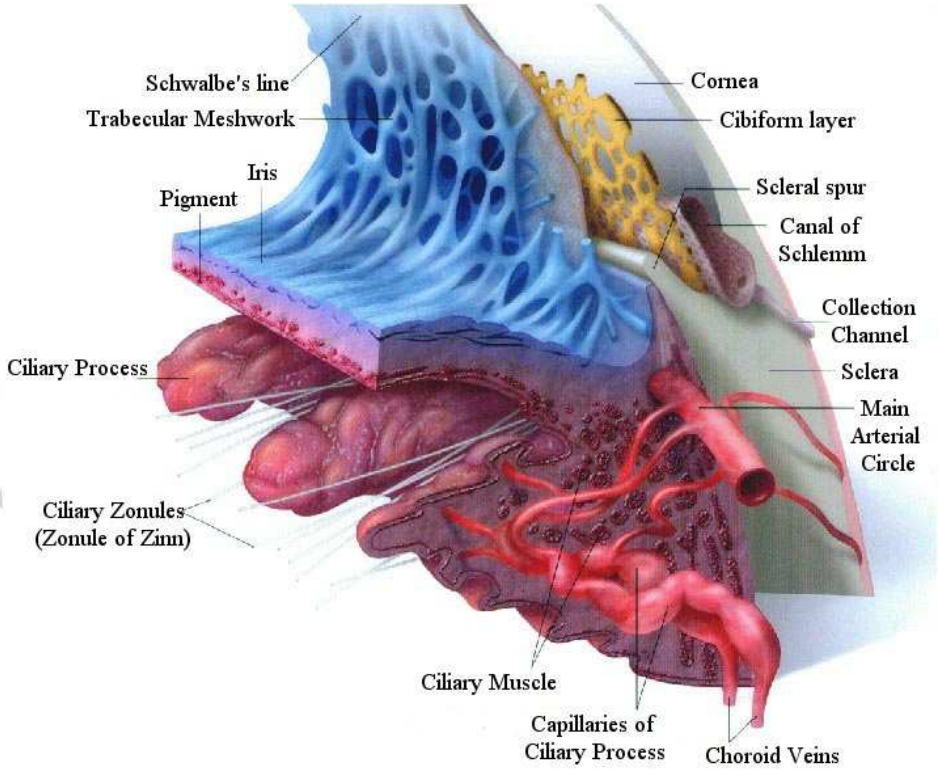

Figure 3.2: A sketch of the connection between the iris, the sclera and the córnea, inside the human eye. The ciliary muscle, responsible to change the lens shape during accommodation, is connected to the lens by the Ciliary Zonules. Source (DECKERT, 2007).

The retina, located in the posterior part of the eye, is the sensory element of the pupillary system, consisting approximately of 130 millions of photo-receptors (rods and cones). It converts electromagnetic radiation, already disturbed by other tissues of the eye, to neural action potentials[2] per unit of time. After the ganglion retinal cells, the pulses pass through sustained X cells, which act as a low-pass filters, and transient Y cells, which are high-pass filters (PRIVITERA; STARK, 2006), and then, they are sent to the brain through the optic nerve (TREVOR-ROPER; CURRAN, 1984). The illuminance

[2]Neural action potentials, in neurophysiology, is a pulse-like wave of voltage that travels along several types of cell membranes inside the optic nerve

reaching the retina is measured in Troland (Td) which means the photo luminance cd/m^2 multiplied by pupil area (m^2).

3.1 The Iris

The human iris has a diameter of about 12mm forming a disc. It controls how much light reaches the retina and divides the two aqueous filled compartments, of the anterior and posterior eye chambers. Under high levels of lighting, the iris dilates, flattening itself and decreasing the pupil size. Under low levels of illumination, it constricts, folding itself and increasing the pupil area. The pupil diameter varies from 1.5mm to 8mm on average (REEVES, 1920), and, in general, it is not a perfect circle. Also, its center may deviate from the center of the iris by an offset of up to 20%, generally to nasal side (FREDDO, 1996).

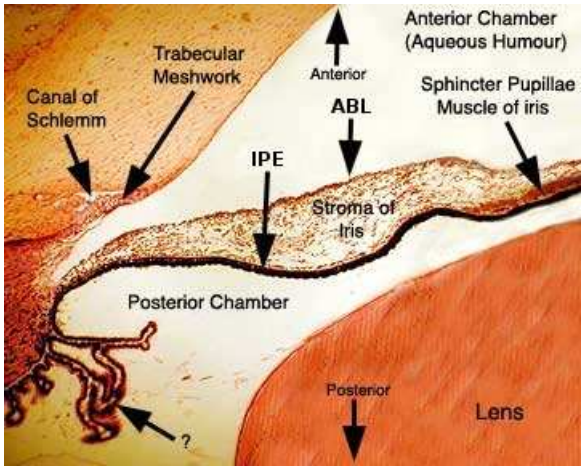

Figure 3.3: A sketch showing the dilator muscle, the sphincter muscle, ABL, Stromal Layer and IPE. Extracted from (BELL, 1999)

As showed in Figure 3.3, the iris is a vascularized structure and consists of three layers: (i) *anterior border layer* (ABL) composed by a dense arrangement of pigmented cells (melanocytes), collagen fibers and fibroblasts; (ii) *stromal layer*, a neuro-vascular tissue very similar to ABL but loosely arranged; and (iii) *iris pigmented epitelium* (IPE), a highly pigmented tissue made with epithelial cells forms an opaque layer (IMESCH; WALLOW; ALBERT, 1997). The color of the iris is determined by the pigmentation density, the quantity of hemoglobins and carotenoids, and the scattering processes in the ABL and stromal layers (*i.e.* blue irises are a result of absorption of long wavelength light and reflection of shorter wavelengths by the iris tissues) (BARANOSKI; LAM, 2007; FREDDO, 1996). Ambient illumination can change the iridal color as showed in Figure 3.4.

The human iris is also divided in two zones by the *collarette*, a delicate zig-zag line also known as the iris frill (Figure 3.5). The *pupillary* zone is the boundary area next to the pupil. The *ciliary* zone extends from the outer border of the iris to the collarette. Each zone is characterized by a muscle in the stromal layer. The *sphincter*, located in the pupillary zone inside the IPE layer and closest to Stroma, is a circumferentially oriented thin smooth muscle that constricts to decrease the pupil size. The *dilator*, found in the ciliary zone, is a radial muscle that constricts to increase the pupil size. Figure 3.5 shows three visible features of the iris, formed by the collagen fibers which have no genetic

Figure 3.4: Two photographs of the same eye under different illumination conditions. The image on the left was taken under natural lighting while the image on right was illuminated with a flashlight.

penetrance[3]: (1) thin regions called crypts (also called Crypts of Fuchs), (2) the collarette and (3) highly dense pigment spots or moles, appearing randomly over the ciliary zone. There are three other visible features: (i) concentric furrows in ciliary zone, folds made by the dilator muscle during the contraction; (ii) radial furrows closest to the pupil and (iii) the pupillary ruff located at the pupillary margin, formed by a visible part of IPE.

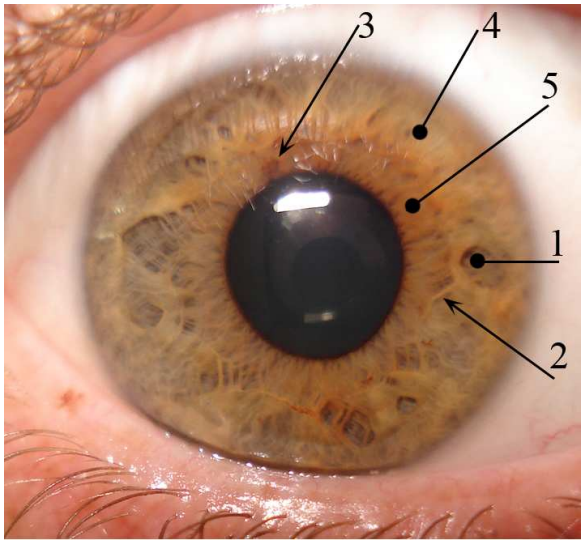

Figure 3.5: Photograph of a human iris. The numbers indicate: (1) crypt, (2) collarette, (3) pigment spot, (4) ciliary zone and (5) pupillary zone.

The sphincter and dilator muscles are independently connected to the autonomous nervous system (ANS) (TILMANT et al., 2003; KRENZ et al., 1985). The sphincter is innervated by parasympathetic nerves (PNS) while the dilator is innervated by sympathetic nerves (SNS). In such an arrangement, the two muscles move autonomously. The parasympathetic and sympathetic pathways are distinct and never cross, so the pupil size results from a balance of the separately incoming stimuli to the two muscles (BERGAMIN et al., 1998). The Parasympathetic neural pathway, for example, starts on the retina, pass

[3]The extent to which a genetically determined condition is expressed in an individual (DAUGMAN, 2002)

through the Edinger-Westphal nuclei and ends on the iris muscle (Figure 3.6) (PRIVITERA; STARK, 2006).

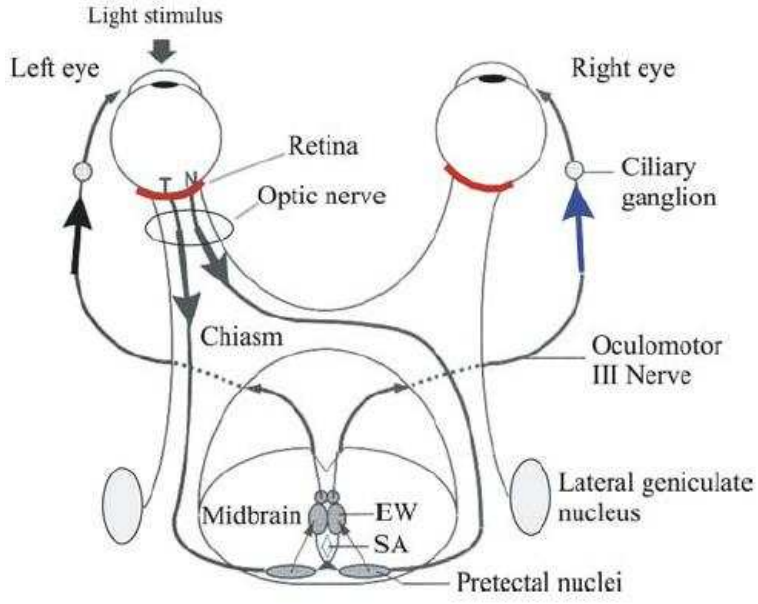

Figure 3.6: Parasympathetic neural pathway of pupil light reflex. The Parasympathetic neural pathway starts on the retina, pass through the Edinger-Westphal nuclei and ends on the iris muscle. Source: (PRIVITERA; STARK, 2006)

The pupil moves in according to two actions: pupil light reflex (PLR), the pupil response for light reaching the retina and accommodation, the pupil response for focal length. There is also some involuntary variation called *hippus*. The ANS conducts the PLR and hippus actions. Accommodation pulses, however, do not affect the iridal muscles directly, only the ciliary muscle, which is located in the root of the iris suspending the lens (TAMM; TAMM; ROHEN, 1992). During PLR, when light reaches the retina, neural signals are sent by the SNS and the PNS pathways to the brain, which sends back a signal for closing or opening the pupil. PLR can be modeled in two phases: perception and, after some time delay, an adjustment. It is also an example of a negative feedback system (PINGNET et al., 1988), since an increase of light will cause a decrease of pupil size.

Several researches found external factors that affect pupil size though PLR, accommodation or hippus: lighting (REEVES, 1920; ELLIS, 1981; STILES; CRAWFORD, 1933; MOON; SPENCER, 1944; POKORNY; SMITH, 1995), focal length (KASTHURIRANGAN; GLASSER, 2005; SCHOR; BHARADWAJ, 2005), spatial patterns in visual field (UKAI, 1985; LI; LIANG; SUN, 2006; LI; SUN, 2005; REEVES, 1920), respiratory and heart rate (YOSHIDA et al., 1994, 1995; CALCAGNINI et al., 2000), particular states of mind and emotional factors, such as interest and curiosity (HESS; POLT, 1964; PEASE; PEASE, 2004), drugs and diseases (BERGAMIN; ZIMMERMAN; KARDON, 2003; KOJIMA et al., 2004), age (STRAUB; THIES; KERP, 1992; WINN et al., 1994), iridal color (BERGAMIN et al., 1998), spectral sensitivity (WERNER, 2003), and even the exact region on the crystalline lens reached by an incident light beam, called Stiles-Crawford effect (STILES; CRAWFORD, 1933). Taking all these aspects into account, when designing a physiologically-based model for the pupil size, seems to be impractical

due to their inherent complexity and limited supporting data.

3.2 Biological Iris Structure Models

Although the iris is a well-known structure in the biological field (FREDDO, 1996), the literature seems to contain no analytical model describing its behavior. According to Wyatt (2000), Rohen (1951) seems to have been the first researcher to study the form of the collagen structure of the iris. He proposed a model for the collagen fibers in which they are arranged in a series of parallel arcs, connecting the iris root with the pupil border, clockwise and counterclockwise in an angle of 90 degrees oriented by the center of the pupil (Figure 3.7). These fibbers are interwoven with other iris components like blood vessels.

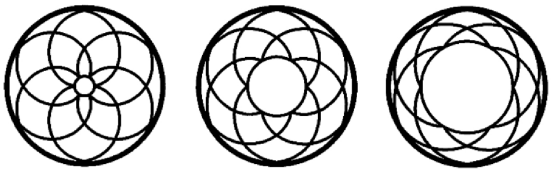

Figure 3.7: The collagen arrangement in a series of parallel arcs model proposed by Rohen (1951). Image source: (WYATT, 2000)

Newsome and Loewenfeld (1971) studied iris details such as the thickness and course of iris vessels, the size and shape of crypts and the position of the folds step by step, from larger to smaller pupils. According to them, there are no observable differences in the iris regarding light-induced or drug-induced pupil dilation/constriction. The ciliary zone grew steadily each step, but in contrast the surface area of the pupillary zone did not change until the pupil is quite small. This means that the ciliary zone is deforms linearly, while the pupillary zone in a non-linear way. They also found lower and higher limits for this non-linearity. However, the article points to possible errors in accuracy, specially when the pupil size is large.

Based on the fibber arrangement proposed by Rohen, Wyatt (2000) derived equations that minimize the wear and tear of the collagen fibbers and created a non-linear 2D mathematical model for iris deformation. However, Wyatt did not consider iridal folds and validated his model with canine, porcine and monkey iris. Although this model was already used by iris recognition systems (WEI; TAN; SUN, 2007; YUAN; SHI, 2005), there are no studies indicating that Wyatt's model can be applied to human iris (WYATT, 2007). Nevertheless, Wei *et al.* (2007) and Yuan (2005) applied the Wyatt's model to human iris recognition systems, reducing the recognition error by 0.2% and 0.3% respectively.

3.3 Summary

This chapter presented a brief overview of the iris structure, and its neural system and actions. Such a description was intended to provide just enough information to familiarize the reader with some concepts and terminology that will be used in the next chapters, such as the notions of pupil light reflex and its associated delay. An in-depth description of these subjects is beyond the scope of this thesis and can be found in many medical literature sources (TREVOR-ROPER; CURRAN, 1984).

4 MODELS OF PUPIL DYNAMICS

This chapter provides an overview of key models designed to assist the analysis of PLR and hippus movements. These models take into account, either explicitly or implicitly, a number of physical parameters related to these phenomena that will be explained in the chapter: (i) *latency*, (ii) the *constriction velocity*; (iii) the *dilation velocity*; (iv) the *maximum pupil size*; and (v) the *minimum pupil size*. The models described here form the basis of the proposed physiologically-based PLR model that will be presented in chapter 5.

4.1 Empirically-Based Models

The pupillometry literature describes several models built around experiments designed to measure the values of some parameters as a function of incident light intensity. Link and Stark (1988) performed a study where a light source was placed in front of the subjects' irises and, by varying the intensity and frequency of the light, they measured the pupillary latency, a time delay between the instant in which the light pulse reaches the retina and the beginning of iridal reaction due nerve transmission, neuro-muscular excitation and activation delays. Their results are summarized in the model represented by Equation 4.1. Incidentally, no information about how many subjects took part in the experiment has been provided.

$$\tau(R, L_{fL}) = 253 - 14\,ln(L_{fL}) + 70R - 29\,R\,ln(L_{fL}) \tag{4.1}$$

where τ is the latency in milliseconds, L_{fL} is the luminance measured in foot-Lambert (fL), and R is the light frequency measured in Hz.

Ellis (1981) performed a similar experiment (without considering the light frequency) with 19 volunteers to find three equations that provide the average latency, and maximum constriction and dilation velocities for a given light source intensity. These equations are given by

$$\tau(L_{cd}) = 445.7 - 22.9L_{cd} + 76.2L_{cd}^2 \tag{4.2}$$
$$V_c(L_{cd}) = 0.15 + 2.0L_{cd} - 0.17L_{cd}^2 \tag{4.3}$$
$$V_d(L_{cd}) = 0.16 + 0.72L_{cd} - 0.07L_{cd}^2 \tag{4.4}$$

where τ is expressed in ms, V_c and V_d are expressed in mm/s, and L_{cd} is the intensity of the light, measured in $candelas/m^2$. Figure 4.1 shows a comparison between the latency models from Ellis (Equation 4.2) and Link and Stark when $R = 0.4$ (Equation 4.1).

Similar models (MOON; SPENCER, 1944; GROOT; GEBHARD, 1952; POKORNY; SMITH, 1995) predict an average pupil size as a function of the light intensity using a

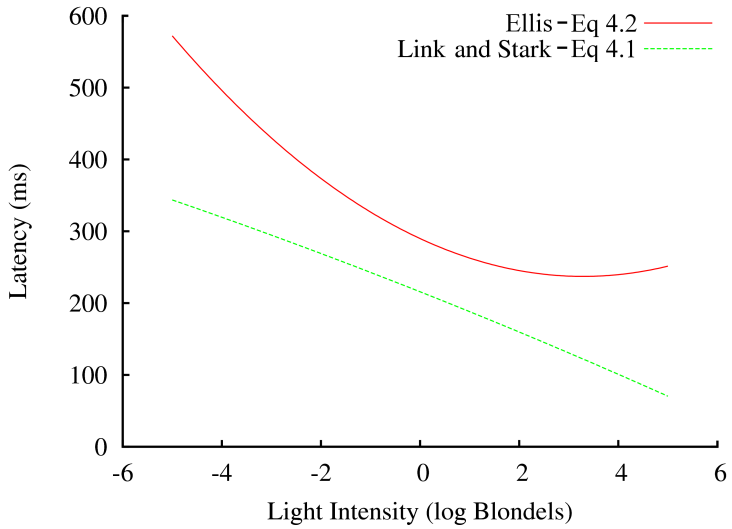

Figure 4.1: Comparison between latency models from Ellis (Equation 4.2) and Link and Stark when $R = 0.4$ (Equation 4.1).

few experimental measurements and previous available data. In those experiments, each subject is seated in front of a white screen which fills most of his/her field of view. The uniform light intensity from the screen affects the pupil diameter, which is measured after the pupil reaches an equilibrium state. For instance, Moon and Spencer (1944) examined the available data and proposed a model for the pupil size of an average subject, that is given by

$$D = 4.9 - 3tanh\left[0.4(log_{10}(L_b) - 0.5)\right] \tag{4.5}$$

where the pupil diameter D varies from 2 to 8mm, and L_b is the background luminance level expressed in Blondels, varying from 10^5 Blondels in sunny days to 10^{-5} Blondels in dark nights. $tanh$ is the hyperbolic tangent. Today, the model proposed by Moon and Spencer is the most cited pupil-size model in the literature.

The de Groot and Gebhard model (1952) was based in experiments involving 43 subjects and is expressed as:

$$D = 10^{(0.8558 - 0.000401(log_{10}(L_a) + 8.1)^3)} \tag{4.6}$$

where the background luminance level L_a is measured in millilamberts (mL). The Pokorny and Smith model is expressed by Equation 4.7:

$$D = 5 - 3tanh(0.4(log_{10}(L_{cd}))) \tag{4.7}$$

Here, the luminance L_{cd} is measured in candelas per square meter (cd/m^2). Figure 4.2 compares the three models.

4.2 Physiologically-Based Models

In Mathematical Biology and related fields, models based on physiological and anatomical observations were derived to express the relationships among the pupillary action variables without relying on quantitative experimental data. For example, Usui and Stark (1982) proposed a parametric model of the iris to describe the static characteristics of pupil response to light stimuli, and to explain its random fluctuations in terms of probability

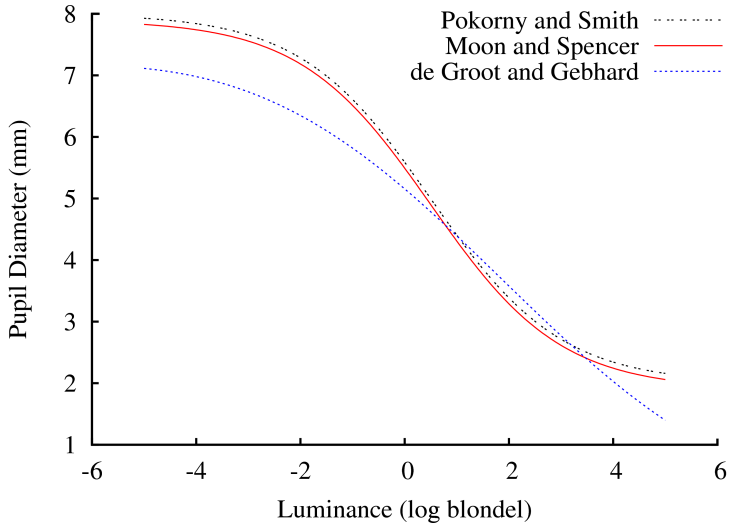

Figure 4.2: Pupil diameter models as a function of luminance expressed in cd/m^2. The compared models are: de Groot and Gebhard (1952), Moon and Spencer (1944), and Pokorny and Smith (1995).

density functions[1]. Recently, Tilmant *et al.* (2003) proposed a model of PLR based on physiological knowledge and guided by experiments. Although they have obtained plausible results, Tilmant *et al.* have recommended the use of another physiologically-based model to monitor more accurately pupillary dynamics, namely the time-dependent model developed by Longtin and Milton (1989), which models the dynamic non-linear behavior of the pupil using a delay-differential equation. Delay-differential equations (DDEs) are a special kind of differential equations whose solutions involve past values of the state variable (NORBURY; WILSON, 2000).

The Longtin and Milton's equation describes the neural ANS pathways, presented in the Section 3.1, to pupillary light reflex. Assuming that all the light reaching the retina is converted to action potentials, Longtin and Milton describe the efferent neural signal $E(t)$ arriving at the iris per unit of time t, as

$$E(t) = \beta \; ln \left[\frac{\phi(t-\tau)}{\bar{\phi}} \right] \tag{4.8}$$

where β is a constant of proportionality and ϕ is the retinal light level measured in lumens and defined by Stark and Sherman (1959) as $\phi = IA$: illuminance (I, in lumens/mm^2) times the pupil area (A, in mm^2), τ is the latency, and $\bar{\phi}$ is the retinal light level threshold (*i.e.*, the light level below which there is no change in the pupil area). The notation $\phi(t-\tau)$ indicates that the current effect depends on the retinal light flux at a time τ units in the past (latency). The delay is calculated with the same physiological parameters using equations presented in the Section 4.1. As the efferent neural signal reaches the iris, it induces some muscular activity x that may cause the pupil to dilate or constrict. According to Partridge and Benton (1981), the relationship between $E(t)$ and x can be approximated by

$$E(t) \tilde{=} k \left(\frac{dx}{dt} + \alpha x \right) \tag{4.9}$$

[1]Probability density functions are functions that represent a probability distribution in terms of integrals

where k is a proportionality factor and α is a rate constant that depends on the definition and units of x used in the model. Longtin and Milton (1989) combine Equations 4.8 and 4.9 as

$$\frac{dx}{dt} + \alpha x = \gamma \; ln \left[\frac{\phi(t-\tau)}{\bar{\phi}} \right] \tag{4.10}$$

They express the pupil area A as $A = f(x)$ and use the inverse $f^{-1}(A) = g(A) = x$ to remove x from Equation 4.10. In their paper, Longtin and Milton use a Hill function (HILL, 1938) (Equation 4.11) as the function f, since it can approximate the elasto-mechanical properties of the iris during the pupillary activity:

$$A = f(x) = \frac{\Lambda \theta^n}{\theta^n + x^n} + \Lambda' \tag{4.11}$$

here, Λ' and $\Lambda + \Lambda'$ are, respectively, the minimum and the maximum pupil areas, and θ is the value of x corresponding to the average pupil area. The Longtin and Milton's model then becomes (LONGTIN; MILTON, 1989):

$$\frac{dg}{dA}\frac{dA}{dt} + \alpha g(A) = \gamma \; ln \left[\frac{\phi(t-\tau)}{\bar{\phi}} \right] \tag{4.12}$$

where

$$g(A) = x = \sqrt[n]{\frac{\Lambda \theta^n}{A - \Lambda'} - \theta^n} \tag{4.13}$$

An S-shaped curve similar to the Hill function has been described in the physiologically-based model of Usui and Stark (1982) to approximate the pupil diameter of an average individual under static illumination conditions.

4.3 Summary

This chapter presented the most important empirical and physiologically-based models for pupil dynamics. Among those, the models of Moon and Spencer, and Longtin and Milton are the most regarded ones in the literature. They form the basis of the proposed physiologically based model that will be described in Chapter 5.

5 THE PROPOSED PHYSIOLOGICAL-BASED MODEL

This chapter presents the main contribution of this thesis: the physiological-based time-dependent model for pupil light reflex, which supports individual differences, and is represented by a delay-differential equation (DDE). The predicted results are compared against videos and photographs from real human irises.

The model of Moon and Spencer (Equation 4.5) is based on a set of discrete measurements and approximates the response on an average individual under various lighting conditions. The measurements have been made after the pupil size has stabilized for each illumination level and, therefore, their model does not describe the pupil behavior outside the equilibrium state. Moreover, pupil size, latency, constriction and re-dilation velocities tend to vary among individuals exposed to the same lighting stimulus (MOON; SPENCER, 1944; WINN et al., 1994), something that is not captured by the model of Moon and Spencer.

Longtin and Milton's model (Equation 4.12) is time dependent and adaptive, with the potential to handle abrupt lighting changes. It is a theoretical model and, unfortunately, Longtin and Milton did not provide the values for the various parameters in their model (*i.e.*, γ, α, θ, n, $\bar{\phi}$), as these, in principle, depend on the abstract notion of iridal muscular activity x, individual differences, as well as on the use of the Hill function. The use of incorrect parameter values will not produce realistic results and may cause Equation 4.12 not to converge.

Starting from the Longtin and Milton's and from Moon and Spencer's models, a practical model that predicts the pupil diameter for the non-equilibrium case based on experimental data is derived (Section 5.2). Section 5.4 shows how the basic model can be extended to take individual variability into account.

The goal is to be able to exploit the flexibility of the Longtin and Milton model while replacing the Hill function with the human-pupil-specific experimental data that forms the basis of the Moon and Spencer model. In order to show how this can be done, a series of algebraic manipulations on the expressions of both models will be made until recover the desired parameter values simply by comparing the two resulting expressions.

5.1 Equilibrium Case

Under constant lighting conditions, the pupil area in the Longtin and Milton's model will converge to an equilibrium state, where

$$\frac{dg}{dA}\frac{dA}{dt} = 0$$

Under such circumstance and assuming there is no occurrence of hippus, ϕ becomes

time invariant. Also, recall that $ln(m/n) = ln(m) - ln(n)$ and, therefore, one can rewrite the Longtin and Milton model (Equation 4.12) for the equilibrium case as:

$$\alpha g(A) = \gamma \, (ln(\phi) - ln(\bar{\phi})) \tag{5.1}$$

In turn, the Moon and Spencer model can be rewritten as

$$\left(\frac{D-4.9}{3}\right) = -tanh\left[0.4\left(\frac{ln(L_b)}{ln(10)} - 0.5\left(\frac{ln(10)}{ln(10)}\right)\right)\right]$$

and since the hyperbolic tangent is an odd function, one can rewrite the above equation as

$$-2.3026 \; atanh\left(\frac{D-4.9}{3}\right) = 0.4(ln(L_b) - 1.1513) \tag{5.2}$$

where $atanh$ is the arc-hyperbolic tangent. Comparing Equations 5.1 and 5.2, in order for the Longtin and Milton's model to fit the response of Moon and Spencer's average subject under the equilibrium conditions, one has

$$-2.3026 \; atanh\left(\frac{D-4.9}{3}\right) \approx \alpha g(A) \tag{5.3}$$

$$0.4(ln(L_b) - 1.1513) \approx \gamma(ln(\phi) - ln(\bar{\phi})) \tag{5.4}$$

From Equation 5.4 one can estimate the value of the parameter γ. One should note that L_b is expressed in Blondels while ϕ is given in lumens. Although, in general one cannot convert between two photometric quantities, this can be done under some well-defined situations (OHTA; ROBERTSON, 2005). Since Moon and Spencer's data were collected with the subject seated before a large white screen of uniform intensity which covers most of their field of view, one can assume that the light reaching a person's pupil has been reflected by a perfect (Lambertian) diffuse surface. Recall that an ideal (loss-less) diffuse reflector returns all of the incident flux so that its reflectance ρ = 1 and its BRDF $f = 1/\pi$ (NICODEMUS et al., 1977). For such a reflector, 1 Blondel = 10^{-6} lumens/mm^2 (OHTA; ROBERTSON, 2005). Since the light flux ϕ depends on the area of the pupil, in order to estimate γ, one first evaluate the left-hand side of Equation 5.4 for the entire range of illumination covered by the Moon and Spencer's model: $L_b \in [10^{-5}, 10^5]$ Blondels. For each value of L_b, one then use Equation 4.5 to estimate D, from which the pupil area $A = \pi(D/2)^2$, and then ϕ, are computed. The retinal light level threshold $\bar{\phi}$ = 4.8118×10^{-10} lumens was obtained using the pupil diameter $D_t = 7.8272$ mm, predicted by Equation 4.5 for $L_b = 10^{-5}$ Blondels. Using the tabulated data for the left-hand side of Equation 5.4 and the conversion scheme just described, one get the following fitting:

$$0.4(ln(L_b) - 1.1513) \approx 0.45 \; (ln(\phi) - ln(\bar{\phi})) - 5.2 \tag{5.5}$$

whose quality of the approximation is illustrated in Figure 5.1 (left). The vertical axis of the graph (scaled muscular activity) represents $\alpha g(A)$, where $g(A) = x$ is the muscular activity. The extra constant -5.2 translates the function on right-hand side of Equation 5.4 vertically, improving the fitting. Given Equation 5.5, one can replace $g(A)$ with $M(D)$ (Equation 5.3), with $\alpha = -2.3026$, where $M(D)$ is given by

$$M(D) = atanh\left(\frac{D-4.9}{3}\right) \tag{5.6}$$

Thus, the equilibrium situation can be expressed by Equation 5.7. As expected, it approximates the Moon and Spencer's function (Equation 4.5) for the pupil diameter of the average subject quite well. The absolute value of the difference between Equations 4.5 and 5.7 is under 2% (Figure 5.2) over the entire range of $[10^{-5}, 10^{5}]$ Blondels (Figure 5.1 right).

$$2.3026\ M(D) = 5.2 - 0.45\ ln\left[\frac{\phi}{\bar{\phi}}\right] \tag{5.7}$$

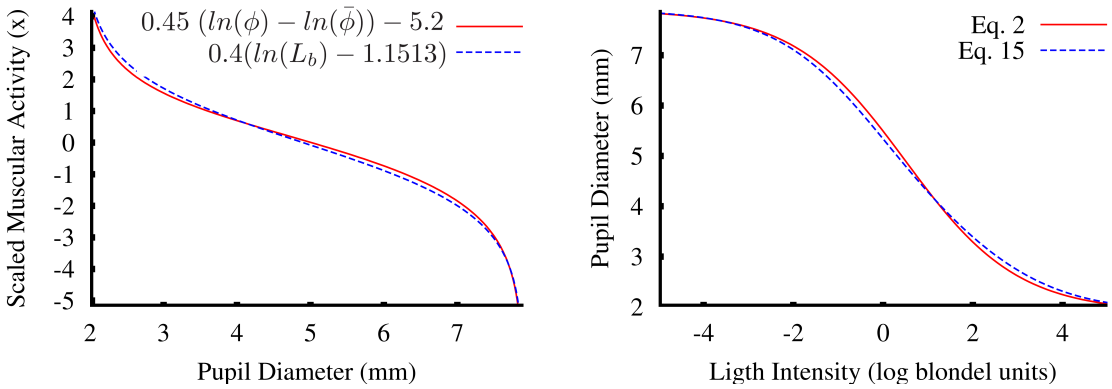

Figure 5.1: High-quality fittings: (left) Both sides of Equation 5.5. (right) Equations 4.5 and 5.7, whose difference in absolute values is under 2% over the entire range $[10^{-5}, 10^{5}]$ Blondels.

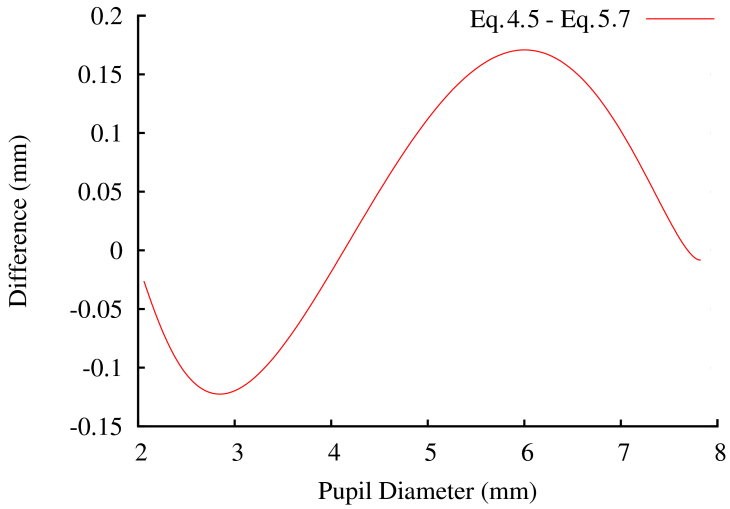

Figure 5.2: Difference between the values predicted by the proposed model and by the Moon and Spencer model. The absolute value of the difference is always less than 2%.

5.2 The Dynamic Case

Equation 5.7 cannot be used to describe the evolution of the pupil diameter in time as a function of instantaneous variations of the light intensity arriving at the pupil. Nevertheless, the obtained constants are still valid for the dynamic case, since the equilibrium

is just a special case of the more general pupil behavior, for which the constants should also hold.

In general, one cannot take an equation obtained for the equilibrium and generalize it to the dynamic case. In the proposed model, however, this is possible because of the following constraints:

- $g(A)$ and $M(D)$ have no explicit time dependence;
- The range of values assumed by A (or D) is the same for both the equilibrium and the non-equilibrium cases;
- There is a one-to-one mapping between A and D.

By introducing time in Equation 5.7, a delay differential equation is obtained that corresponds to the proposed solution for the dynamic case:

$$\frac{dM}{dD}\frac{dD}{dt} + 2.3026\ atanh\left(\frac{D-4.9}{3}\right) = 5.2 - 0.45\ ln\left[\frac{\phi(t-\tau)}{\bar{\phi}}\right] \tag{5.8}$$

where D and ϕ are expressed in mm and lumens, respectively. For latency τ, one use Equation 4.1 noting that 1 Blondel = 0.0929 fL. Pupil constriction velocity is approximately $3\times$ faster than (re)dilation velocity (ELLIS, 1981; BERGAMIN et al., 1998). This difference is took into account by using different time steps for constriction (dt_c) and dilation (dt_d) in the numerical solver simulation:

$$dt_c = \frac{T_c - T_p}{S} \qquad dt_d = \frac{T_c - T_p}{3S} \tag{5.9}$$

where dt_c and dt_d are measured in milliseconds, T_c and T_p are respectively the current and previous simulation times (times since the simulation started) measured in milliseconds, S is a constant that affects the constriction/dilation velocity and varies among individuals. The higher the S value, the smaller the time step used in the simulation and, consequently, the smaller the pupil constriction/dilation velocity.

Figure 5.3 shows the evolution of the pupil diameter for the Moon and Spencer's average subject simulated using Equation 5.8 considering some abrupt changes in the environment luminance. The results are compared to the static models of Moon and Spencer (Equation 4.5) and of de Groot and Gebhard (1952). Note the smooth variation in pupil diameter and the latency (τ) included in the model.

5.3 Solving Delay Differential Equations

Techniques for solving DDEs are well known and several solvers have been implemented using explicit Runge-Kutta methods (SULEIMAN; ISLMAIL, 2001; GUILLOUZIC; HEUREUX; LONGTIN, 1999; PAUL, 1992). However, as the proposed model is bounded by finite limits and the pupil diameter is always positive, a simple interactive numerical solution can solve the Equation 5.8 in real time, which is important for interactive applications, such as video games. A linear iterative convergence process was implemented which, given an initial solution and a time step (dT), approximates D by varying dD until $D_t \approx D_{t-1} + dD$. Algorithm 1 shows a pseudocode of the solver applied to Equation 5.8, considering latency as Equation 4.1 and velocities as an approximation to Equations 4.3 and 4.4.

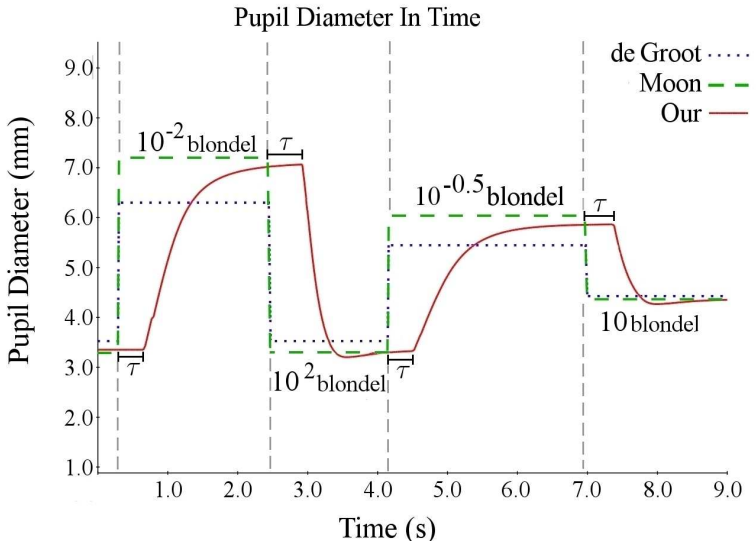

Figure 5.3: Simulated results produced by the proposed model (Equation 5.8) for the average subject of Moon and Spencer under non-equilibrium conditions (solid line). These results are compared to the static models of Moon and Spencer (1944) (dashed line), and of de Groot and Gebhard (1952) (dotted line). Note the latency (τ) predicted by the proposed model and the smooth variation in pupil diameter.

5.4 Modeling Individual Differences

While Equation 5.8 simulates dynamic pupil behavior, it only does so for the average individual represented by the Moon and Spencer model. There are, however, substantial differences in the way pupils from different individuals react to a given light stimulus. Such variations include differences in diameter (CRAWFORD, 1936; MOON; SPENCER, 1944; GROOT; GEBHARD, 1952; ELLIS, 1981; WINN et al., 1994), latency, and constriction and re-dilation velocities (ELLIS, 1981; BERGAMIN et al., 1998). In order to simulate individual differences, one cannot just arbitrarily change the parameter values of the model, as Equation 5.8 may not converge.

Figure 5.4 shows the original data used by Moon and Spencer (1944). The curve C_m (shown in black) was obtained by converting the values of L_b in the range of $[10^{-5}, 10^5]$ Blondels to lumens (see Section 5.1) and then using Equation 5.7 to compute the corresponding pupil diameter values used for plotting. The top and bottom curves, C_t and C_b, respectively, define an envelope containing all pupil diameter values used by Moon and Spencer. C_b was obtained by fitting a 5 degree polynomial to 11 of the smallest pupil diameter values along the entire luminance range. Likewise, C_t was obtained by fitting a 5 degree polynomial to 11 of the largest pupil diameter values. C_b, C_m and C_t are treated as isocurves $C(p)$ for some parameter $p \in [0, 1]$, so that $C(0) = C_b$, and $C(1) = C_t$. The individual differences is then modeled by associating to each individual I a random number $r_I \in [0, 1]$ that corresponds to an isocurve $C(r_I)$. To avoid convergence problems and still achieve the results corresponding to isocurve $C(r_I)$, C_t and C_b are rewitten,

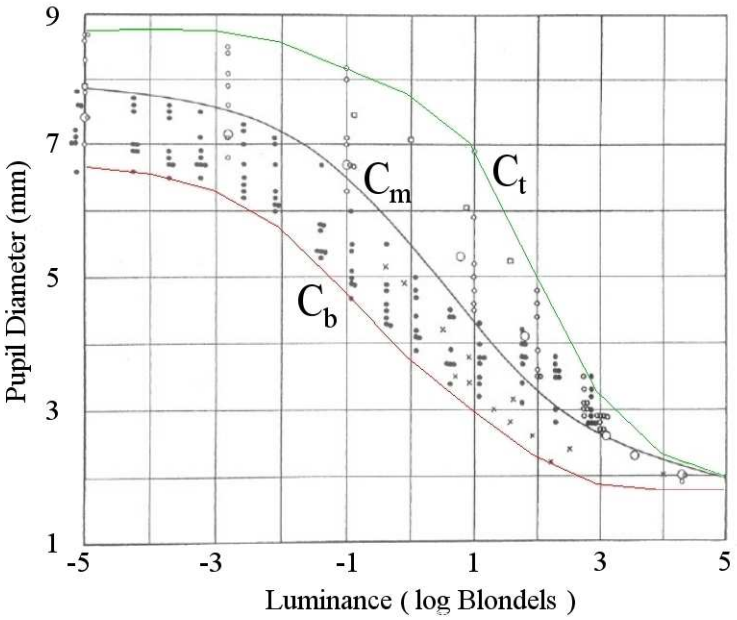

Figure 5.4: Original data used by Moon and Spencer (1944). The curve C_m corresponds to Equation 5.7. The pair of curves C_b and C_t define an envelope containing all data.

respectively, as new functions C_{tD} and C_{bD} of the pupil diameter:

$$\begin{aligned} C_{tD}(D) &= -0.013D^5 + 0.322D^4 - 3.096D^3 \\ &\quad +13.655D^2 - 25.347D + 18.179 \\ C_{bD}(D) &= -5.442D^5 + 1.387D^4 - 1.343D^3 \\ &\quad +6.219D^2 - 1.317D + 1.219 \end{aligned}$$

In order to obtain C_{tD}, the functions C_m and C_t for L_b are evaluated in the range $[10^{-5}, 10^5]$ Blondels, creating ordered pairs of diameter values $(D_m, D_t) = (C_m(L_b), C_t(L_b))$. Given enough of these pairs, a curve was fitted expressing D_t as a function of D_m (or D for short). The resulting curve is C_{tD} (Equation 5.10). The case of C_{bD} is similar. The final pupil diameter at any time is then obtained solving Equation 5.8 for D and then evaluating

$$D_{final} = C_{bD}(D) + (C_{tD}(D) - C_{bD}(D))r_I \tag{5.10}$$

This solution was adopted due to its simplicity and generality: one can easily replace the curves $C_{bD}(D)$ and $C_{tD}(D)$ with new ones, covering new data as they become available, or representing other models (*e.g.*, de Groot and Gebhard (1952)). Since the relative distances of C_m to C_b and C_t vary for different values of D, no value of r_I will exactly recover C_m. This is not a problem, however, as C_m correspond to the average subject. Other parameterizations are possible, including ones that interpolate C_m for a given value of the parameter p.

Although the proposed model properly simulates the elastic behavior of the iris muscular activity during changes in lighting conditions, it does not model hippus (*i.e.*, Equation 5.8 will converge to some pupil diameter value if the lighting conditions remain constant). As random fluctuations whose causes are still unknown (UKAI; TSUCHIYA; ISHIKAWA, 1997), it is currently not possible to define a physiologically-based model for hippus. The hippus effect was visually approximated by adding some small random variations to the light intensity (between $10^{-0.3}$ and $10^{0.3}$ Blondels), to induce small variations

in the pupil diameter (of the order of 0.2 mm (HACHOL et al., 2007)), in the frequency range of 0.05Hz to 0.3Hz. This significantly improves the realism of the resulting simulations and animations in indoor scenes. The high luminance usually found in outdoor scenes tend to constrict the pupils and prevent the occurrence of noticeable hippus.

5.5 The PLR Model Validation

In order to validate the PLR model under non-equilibrium conditions and to show that it is capable of representing individual variability, some qualitative comparisons were performed between actual pupil behavior and the results of simulations produced by the model. For this, videos of normal subjects presenting significantly different light sensitivities (*i.e.*, different PLR responses), were captured while a light was turned *on* and *off* several times. Since pupil constriction is bigger when both eyes are stimulated (THOMSON, 1947), the subjects kept both eyes opened. To avoid fatigue and habituation of the iris (LOWENSTEIN; LOEWENFELD, 1964), less than one minute of video per subject was recorded.

Lighting measurements made during video capture were used as input to the PLR model for simulating pupil behavior. The pupil diameters resulting from these simulations were then compared to the pupil diameters computed at individual video frames. The subjects' pupil diameter were measured at each frame of the video sequences. Note that the simulated results are not expect to quantitatively match the observed ones, but rather be in qualitative agreement with observed behavior.

The videos were captured using a Cannon ELURA2 miniDV camcorder (NTSC, 720×576 pixels) with progressive scan connected to a PC through a firewire connection. The room's light was kept dimmed so that the subjects' pupils could dilate naturally to some extent, but not too dark that one could not see the pupils in the individual video frames. Because of these constraints, only two male subjects (a 24-year-old with green eyes, and a 26-year-old with blue eyes) with light eyes were used. For each frame, the pupil diameters were estimated from the set of dark pixels (pupil area P_{area}) inside a specified rectangle containing solely the subject's pupil and part of the iris (Figure 5.5). Given P_{area}, the pupil diameter was obtained (assuming the pupil is a circle) as $d = 2(\sqrt{P_{area}/\pi})$ pixels. The conversion from pixels to millimeters was performed considering a typical iris diameter of $12\ mm$. Computing the pupil diameter as described produces more accurate results than computing it as the number of pixels in the largest straight segment in the set of dark pixels (the pupil).

Since the video frames were captured at approximately 30 Hz, in practice no variation is expected between the pupil diameters in neighbor frames under constant illumination, even in the presence of hippus. The average error in the computed pupil diameters is approximately $0.1\ mm$ by computing the average difference between estimated pupil diameters for neighbor frames. Based on the video sequences, S was set to 600 (Equation 5.9) for the two subjects in all experiments. This value made their simulated constriction velocities approximate the ones in the video sequences. The frequency of the two light sources in silumations were empirically set to $R = 0.4\ Hz$, a value that made the latency estimated by Equation 4.1 approximate the latency observed in the video frames.

The simulations were evaluated by experiments with both subjects using two different kinds of light sources to induce pupil constriction: a small flashlight and a 100 Watt incandescent white light bulb. For light measurements, a LD-200 Instrutemp digital lux meter (precision $\pm 3\%$, frequency 2Hz) was used.

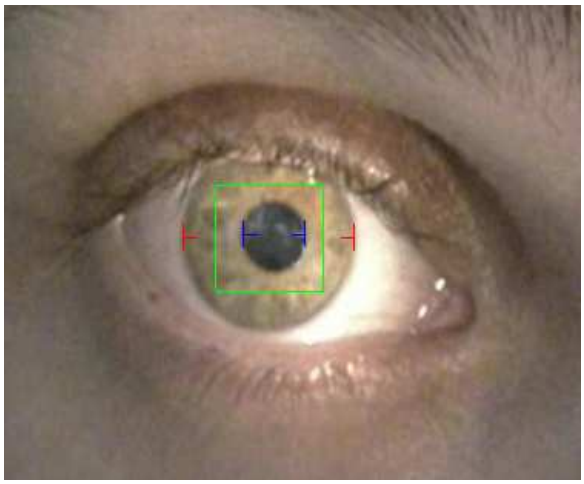

Figure 5.5: Estimating pupil diameter from a rectangular region containing only the pupil and some iris pixels. The pupil diameter is estimated from the area occupied by the dark pixels, assuming a circular pupil and an iris with diameter of 12 mm.

5.5.1 The Flashlight Experiments

In these experiments, a light source induces significant changes in the subjects' pupil diameters without introducing considerable changes in the environment lighting conditions. For this purpose, a small flashlight powered by a single AAA battery (1.5 Volt) was kept at about 20 cm from the subject's right eye and pointed at it. Given the small area illuminated by the flashlight as well as it reduced power, the readings from the lux meter were very sensitive to even small changes in the relative position and orientation of the flashlight with respect to lux meter sensor. Thus, two simulations were runned using the recorded data: (i) considering the light intensity estimated using Equation 4.5, and (ii) considering the readings from the lux meter. These two experiments are explained next.

The first flashlight experiment: In this experiment, the Moon and Spencer equation (Equation 4.5) estimated the light intensities during the *on* and *off* states of the flashlight, based on the measured pupil diameters (from the video). Since the Moon and Spencer function (curve C_m in Figure 5.4) represents the pupil behavior of an average individual, the *on* (*off*) light intensity were estimated as the average of the computed *on* (*off*) intensities for both subjects. Using this procedure, one was obtained $10^{1.1}$ blondels when the flashlight was on, and $10^{-0.5}$ blondels when the flashlight was off. Given the average luminance value for the *on* (*off*) state and the corresponding pupil diameter for a given subject, the inverse of Equation 5.10 estimated the $r_{I_{on}}$ ($r_{I_{off}}$) index for that subject. The subject's final r_I index was computed as the average between his $r_{I_{on}}$ and $r_{I_{off}}$ indices. Using this procedure, one was obtained $r_I = 0.4$ for the green-eye subject and $r_I = 0.03$ for the blue-eye subject.

Figure 5.6 shows the actual pupil diameter measurements performed on a frame-by-frame basis along 9-second-long sequences captured for each subject. The green '+' marks on top represent the measurements for the green-eye subject, while the blue 'x' marks show the measurements of the blue-eye subject. This example illustrates the inter-subject variability in terms of light sensitivity and shows the ability of the model to appropriately represent such individual differences. The vertical dotted lines delimit the intervals in which the flashlight was kept on and off for each subject. The solid and

dashed lines represent the simulated results produced by the model for the green-eye and blue-eye subjects, respectively, and closely agree with the actual measured values. These curves were produced automatically from Equations 5.8 and 5.10, on top of which small random variations (hippus effect) are added as described in the previous section. The accompanying video shows side-by-side comparisons of the simulated results and videos captured for the two subjects.

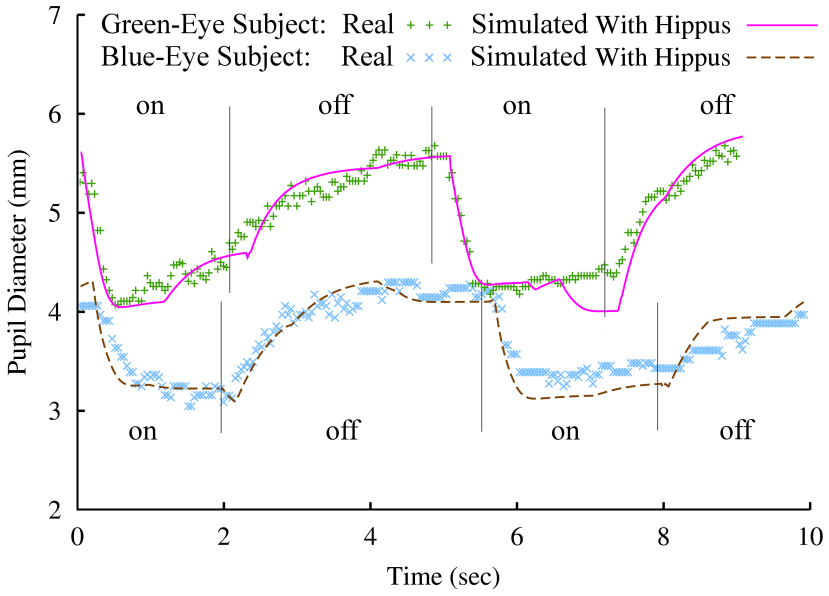

Figure 5.6: Comparison between the simulated results and measurements from real video sequences using the flashlight as stimulus. The green '+' and the blue 'x' marks represent, respectively, the pupil diameter measurements for the green-eye and for the blue-eye subjects, obtained for all frames along a 9-second-long video sequence. The solid and dashed lines are the pupil diameters predicted by the physiologically-based model for the green-eye and for the blue-eye subjects, respectively, after random noise (hippus effect) has been added. The vertical dotted lines delimit the intervals in which the flashlight was kept on and off for each subject. The predicted values closely agree with the actual measured values.

The second flashlight experiment: In this experiment, the readings provided by the lux meter for the *on* and *off* states of the flashlight were used. These illuminance values were 350 lux[1] and 90 lux, respectively. One should recall that in such a setup, small changes in the position and orientation of the subject's head produce changes in the illuminance at the pupil. Therefore, these values are only approximations to the actual illuminance reaching each subject's lit eye. Given the illuminance values and the subjects' corresponding pupil diameters estimated from the video frames, the actual pupil's luminous flux (in lumens) was obtained at the two flashlight states, for each individual. These values were then converted to blondels according to the assumption described in Section 5.1. Equations 5.8 and 5.10 estimated their corresponding r_I indices (by averaging $r_{I_{on}}$ and $r_{I_{off}}$), obtaining $r_I = 0.54$ for the blue-eye subject and $r_I = 0.92$ for the green-eye subject. Figure 5.7 compares the actual pupil measurements (same as in Figure 5.6) with the results simulated by the model using the lux meter readings as input. The differences between the simulated curves shown in Figure 5.6 and 5.7 are primarily due to the added random noise (hippus).

[1] $1\ lux = 1\ lumen/m^2$

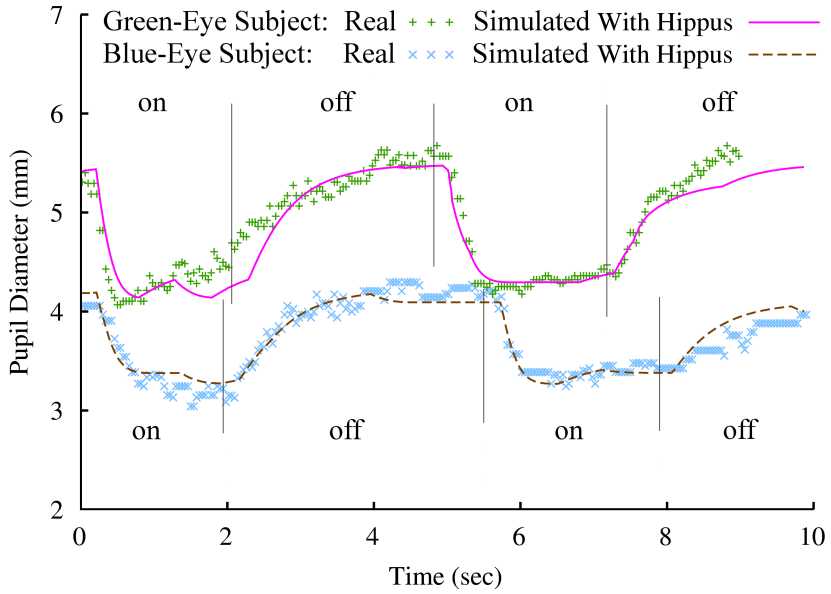

Figure 5.7: Similar to the graphs shown in Figure 5.6 but using the illuminance readings provided by the lux meter as input to the model. The simulated results, including hippus, for the green-eye and blue-eye subjects are shown as solid and dashed lines, respectively.

5.5.2 The 100 Watt Lightbulb Experiment

For this experiment, a more stable light source to induce pupil constriction was used: a spot with a 100 Watt incandescent white lightbulb, kept at about one meter in front and one meter to the right of the subject's head. This setup allowed the subjects to remain comfortable with their eyes opened while the light was on.

The environment light intensity was measured during the *on* and *off* states by positioning the digital lux meter at approximately the same position and orientation of the subject's right eye. During the blue-eye subject experiment, the illuminance was 140 lux when the light was off and 315 lux when it was on. During the green-eye subject experiment, the readings were 91 and 540 lux, respectively. These differences resulted from a darker environment and a slight approximation of the green-eye subject to the light source. Again, the illuminance values and the subjects' corresponding pupil diameters (measured from the video) were used as input to Equations 5.8 and 5.10 to estimate their corresponding r_I indices (by averaging $r_{I_{on}}$ and $r_{I_{off}}$). One was obtained $r_I = 0.9$ for the blue-eye subject and $r_I = 1.0$ for the green-eye subject.

Figure 5.8 (top) shows the actual pupil diameter measurements performed on a frame-by-frame basis along 56 and 50-second-long sequences captured for the blue-eye and for the green-eye subjects, respectively. The vertical lines delimit the intervals in which the light was kept *on* and *off* for each subject. The solid and dashed lines represent the simulated results produced automatically by the proposed model (Equations 5.8 and 5.10) with and without hippus, respectively, and closely agree with the actual measurements. Figure 5.8 (bottom) shows zoomed versions of portions of the graphs shown on top, exhibiting *off-on-off* transitions.

One should note that the simulated results produced by the PLR model closely approximate the actual behaviors of the subjects' pupils in all three experiments, illustrating the effectiveness of the model. The differences in the r_I indices for a given subject among the experiments can be explained as:

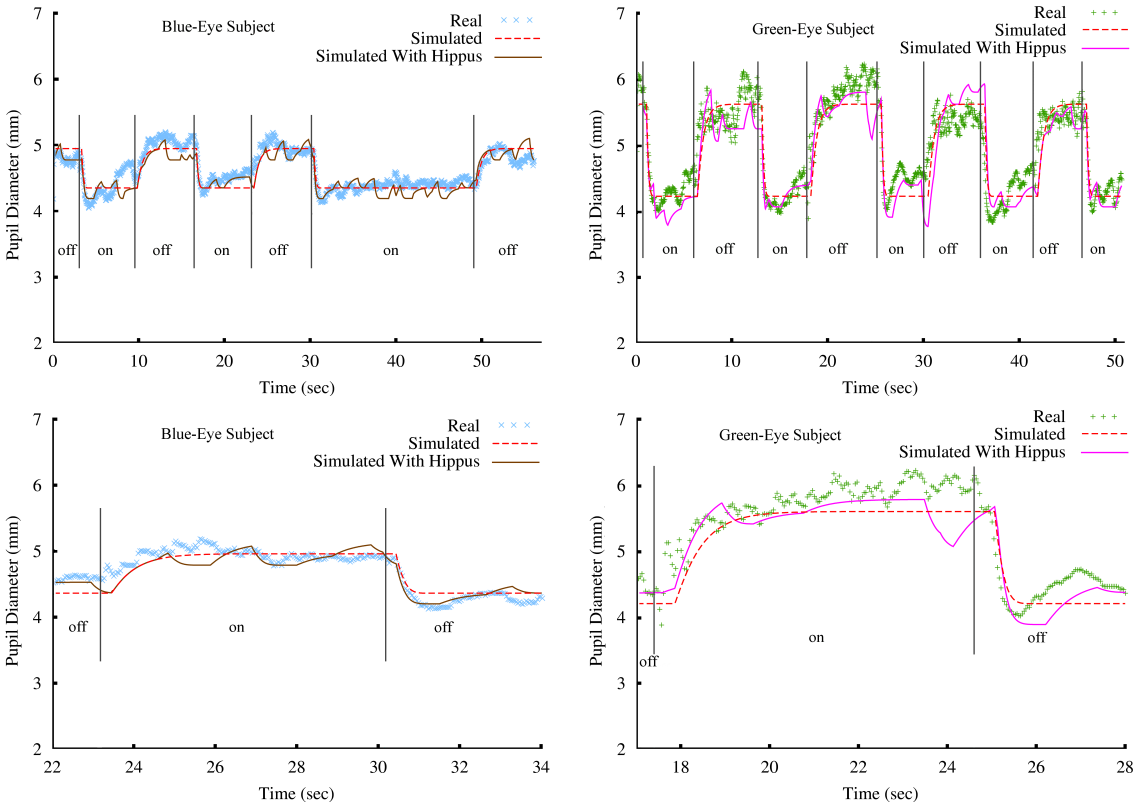

Figure 5.8: Comparison between the simulated results and measurements from real video sequences using light emitted by a lightbulb as stimulus. The 'x' and '+' marks represent the pupil diameter measurements for the blue-eye (left) and for the green-eye (right) subjects, respectively. Top row: values obtained for all frames along a 56- and 50-second-long video sequence, respectively. The solid and dashed lines are the pupil diameters predicted by the physiologically-based model with and without hippus, respectively. The vertical lines delimit the intervals in which the incandescent light bulb was kept on and off for each subject. The predicted values match the actual measurements well. The bottom row shows zoomed versions of the graphs shown on the top.

- In the two flashlight experiments, the pupil diameters used for the *on* and *off* states were the same, but the illuminance values provided by Equation 4.5 and by the lux meter were different. The different indices simply reflect the different light sensitivities presented to the model as input;

- When comparing the 100 Watt lightbulb and the flashlight experiments, both the lighting and the pupil sizes varied for the *on* and *off* states of the light sources. For instance, for the green-eye subject, the pupil diameters were approximately 4.3 mm and 5.7 mm for the *on* and *off* states of the flashlight, respectively (Figure 5.7). This resulted in a r_I index of 0.92. In the case of the 100 Watt lightbulb experiment, these values were approximately 4.3 mm and 6.0 mm, respectively (Figure 5.8), with r_I = 1.0. These two indices are relatively close and reflect the difference in the maximum pupil diameters between the two experiments. The difference in the r_I indices for the blue-eye subject were considerably bigger, from 0.54 to 0.9. Again, this can be explained by comparing the measured pupil diameters in the two experiments. These values went from approximately 3.2 mm and 4.2 mm in the *on* and *off* states

of the flashlight (Figure 5.7) to 4.4 mm and 5.2 mm in the *on* and *off* states of the 100 Watt lightbulb (Figure 5.8).

An important point to note is that by using an average of the estimated r_I indices for the *on* and *off* states of the light source, the proposed model is capable of realistically simulating the pupil behavior of individuals with considerable differences in PLR responses under different and variable lighting conditions.

5.6 Using de Groot and Gebhard Data

The de Groot and Gebhard average subject (Equation 4.6) differs from Moon and Spencer's (Equation 4.5 - Figure 4.2), but one can adapt Equation 5.8 to approximate de Groot and Gebhard's model. In fact, one can map the results of the proposed model to any other. In this case, one first compute the diameter differences between the two empirical models for the light intensity range:

$$D_{diff}(L_b, L_a) = D_{moon}(L_b) - D_{groot}(L_a) \tag{5.11}$$

where D_{moon} is Equation 4.5, D_{groot} is Equation 4.6, L_b is the luminance measured in Blondels and L_a the luminance in millilamberts. One then fits a polynomial to the values of D_{diff} and approximates $D_{groot} = D_{moon} - D_{diff}$. From this relation, one gets:

$$\begin{aligned} D_{groot}(D_{moon}) &= D_{moon} \\ &+ 0.0054820\, D_{moon}^5 \\ &- 0.14309\, D_{moon}^4 \\ &+ 1.481\, D_{moon}^3 \\ &- 7.6023\, D_{moon}^2 \\ &+ 19.032\, D_{moon} \\ &- 18.096 \end{aligned} \tag{5.12}$$

The Equation 5.7 is then adapted to approximate Groot and Gebhard's model.

$$2.3026\ atanh\left(\frac{D_{groot}(D) - 4.9}{3}\right) = 5.2 - 0.45\ ln\left[\frac{\phi(t-\tau)}{\bar{\phi}}\right] \tag{5.13}$$

where $\phi(t) = A(t) * I(t) = area(D(t)) * I(t)$ as $\phi = area(D_{groot}(D(t))) * I(t)$.

The graph in Figure 5.9 compares the models of Moon and Spencer (green dashed line) and de Groot and Gebhard (red line), The graph also shows the difference between the two models (double dotted brown line), and the evaluation of Equation 5.12 using the diameter from Equation 5.8 in equilibrium (dotted blue line). As one can see, the model was adapted to reach the same pupil diameter of de Groot and Gebhard average subject. Assuming the constraints discussed in Section 5.2, the equation can be extended to the dynamic case:

$$\frac{dM}{dD}\frac{dD}{dt} + 2.3026\ atanh\left(\frac{D_{groot}(D) - 4.9}{3}\right) = 5.2 - 0.45\ ln\left[\frac{\phi(t-\tau)}{\bar{\phi}}\right] \tag{5.14}$$

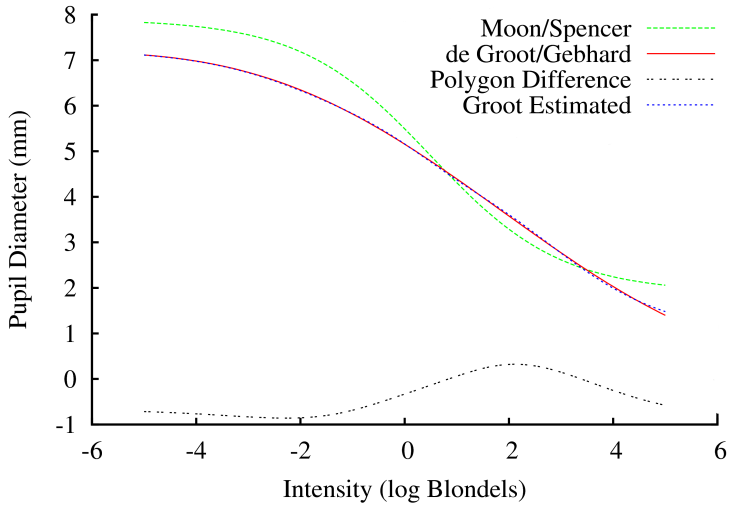

Figure 5.9: The proposed model simulating de Groin and Gebhard data. Models of Moon and Spencer (Green line) and de Groot and Gebhard (Red line), the function difference between them (Brown line), and the evaluation of Equation 5.12 using the converged values from Equation 5.8.

5.7 Summary

This chapter proposed a physiological-based time-dependent model for pupil light reflex and an extension to handle individual variability, hippus, latency and velocity models. It also discussed a way to implement a DDE solver for the proposed model. The implementation of the model runs in real-time, predicting smooth variation of the pupil diameter under variable lighting conditions. The results of the model closely agree with the real data, captured from two subjects.

Algorithm 1 Pupil Diameter at Light Intensity

Require: $intensity$ {Light intensity}
Require: $time$ {Time}
Require: $history$ {Initial state in tuples (time,intensity,diameter)}
Require: S {Constant for constriction/dilation velocity}

$\tau \leftarrow getLinkAndStarkLatencyFor(intensity)$ {Equation 4.1}
$tuple \leftarrow history.get(time - \tau)$
$rightValue \leftarrow evaluateRightSideOfEquation5.8(tuple)$

$dD \leftarrow 0$
$step \leftarrow 10$;

{100 iterations are enough}
for $0...100$ **do**
  $dT \leftarrow (time - history.last().time)/S$

  if $dD > 0$ **then**
    $dT \leftarrow dT/3$ {if dilating decrease the velocity}
  end if

  $leftValue \leftarrow evaluateLeftSide(dD, dT, diameter)$

  if $leftValue = rightValue$ **then**
    return $history.last().diameter + dD$
  end if

  if $leftValue$ is **not** getting closer to $rightValue$ **then**
    $step \leftarrow -step/2$ {Invert and decrease the size of step}
  end if

  $dD \leftarrow dD + step$
end for

return history.last().diameter {If here, the process did not converge}

6 MODELING THE IRIS DEFORMATION

This chapter describes the second contribution of this thesis: an image-based model for iridal pattern deformation obtained from the analysis of several high-resolution pictures and videos taken from nine volunteers with different induced pupil sizes. A comparison of the model renderings with photographs evaluates the model.

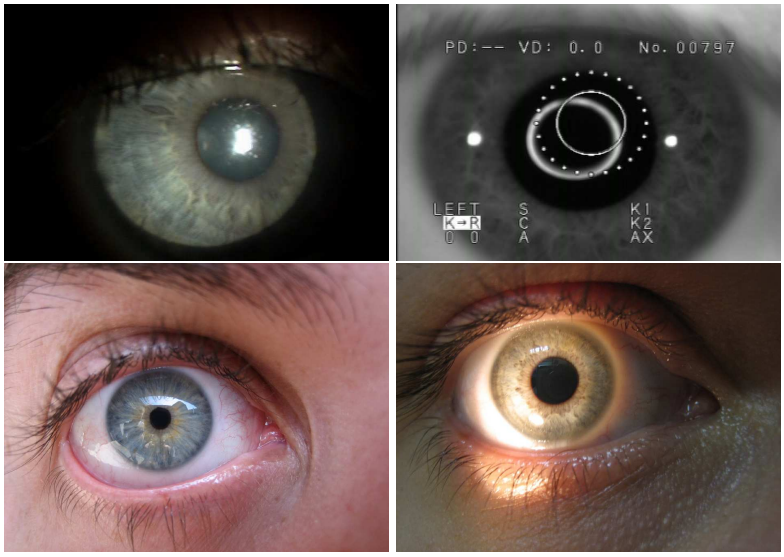

Figure 6.1: Sample images from the four devices used to capture iris deformation. (top) Two keratometers images: (top-left) at UFRGS University Hospital and (top-right) at USP/SC Optics Department. (bottom) Photographs of the irises from two subjects.

As the pupil diameter varies, the iridal patterns deform accordingly. Although the iris is a well-known structure in the Biology/Medical literature (FREDDO, 1996), there is no general agreement about a model of its behavior. This thesis derive a model for iridal pattern deformation by analyzing sets of photographs taken from volunteers under controlled conditions. In the beginning of the work two keratometers were used instead of digital cameras, but their images had limited resolution, generally they were out of focus and one of devices could not capture the entire iris surface simultaneously (Figure 6.1 top-left). Images taken with digital cameras can achieve better focus and image resolution, but tend to have more corneal reflection (Figure 6.1 bottom). Nevertheless, the images taken with digital cameras were better suited to track the iris patterns.

In the experiments, an eye doctor dilated the pupils of four volunteers with some mydriatic drug and one person photographed their irises at several stages during the pupil dilatation process using a Canon PowerShot SD 400 camera with macro lens. The images

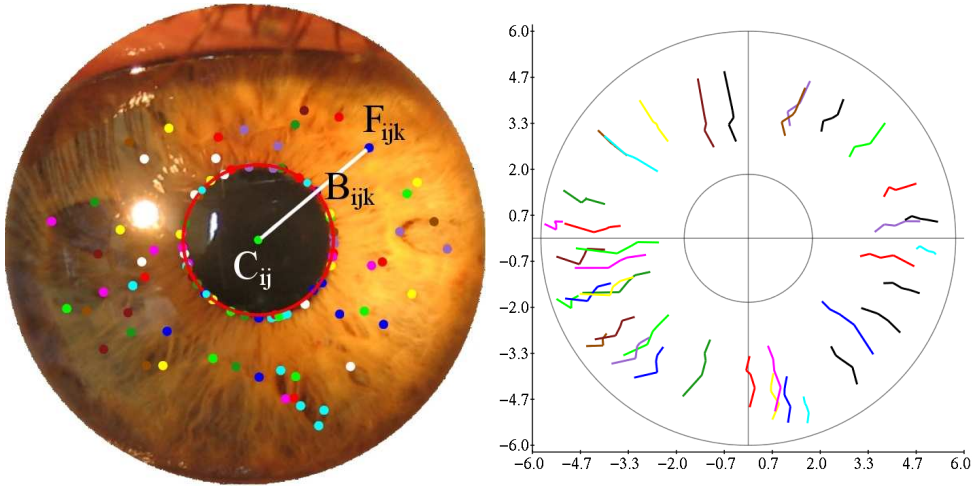

Figure 6.2: Left: Photograph of a volunteer's iris taken during the dilation process. The color dots indicate tracked points F_{ijk}, the center of the pupil C_{ij}, and the border positions B_{ijk} associated with feature points F_{ijk}. A red circle approximates the pupil. Right: Evolution of the positions of the 50 individually tracked iridal features during the dilation process. Each feature is identified by a different color. Note that for better contrast the color of white dots was changed to black lines.

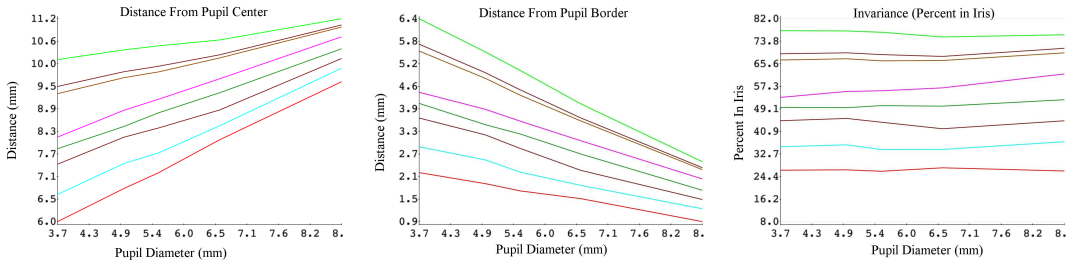

(a) (b) (c)

Figure 6.3: Measured values for some tracked feature points along the dilation process. (a) Distance from F_{ijk} to C_{ij}. (b) Distance from F_{ijk} to the B_{ijk}. (c) Ratio between the distance from F_{ijk} to the B_{ijk} and the local width of the iridal disk. To a first approximation, one can assume that the first two measurements vary linearly, while the third one is constant.

were taken at the resolution of 2,048 $\times$ 1,536 pixels, and were then cropped to square images containing only the iris and pupil. After cropping, the smallest image was 800 $\times$ 800 pixels and the larger ones were rescaled to fit the same dimensions. Thus, let $S_i = \{I_{i1}, I_{i2}, ..., I_{in}\}$ be the set of n images from a given volunteer V_i taken along the process, sorted by pupil diameter, for each image I_{ij}, a circle on the outer border of the iris and another one at the border of the pupil were positioned (the two circles delimit the iridal disk). The center of the pupil C_{ij} was marked as the center of the inner circle and, after it, a series of iridal features $\{F_{ij1}, F_{ij2}, ..., F_{ijm}\}$ were marked and tracked along the set of images of each volunteer. Since the inner circle is only an approximation to the pupil border and that the center of the pupil does not necessarily coincide with the center of the iris (Section 3.1), each tracking point F_{ijk} was adjusted the pupil border position B_{ijk} along the segment $F_{ijk} - C_{ij}$. Figure 6.2 (left) shows an image with the tracked features F_{ijk} indicated by a set of colored dots, the approximated pupil border

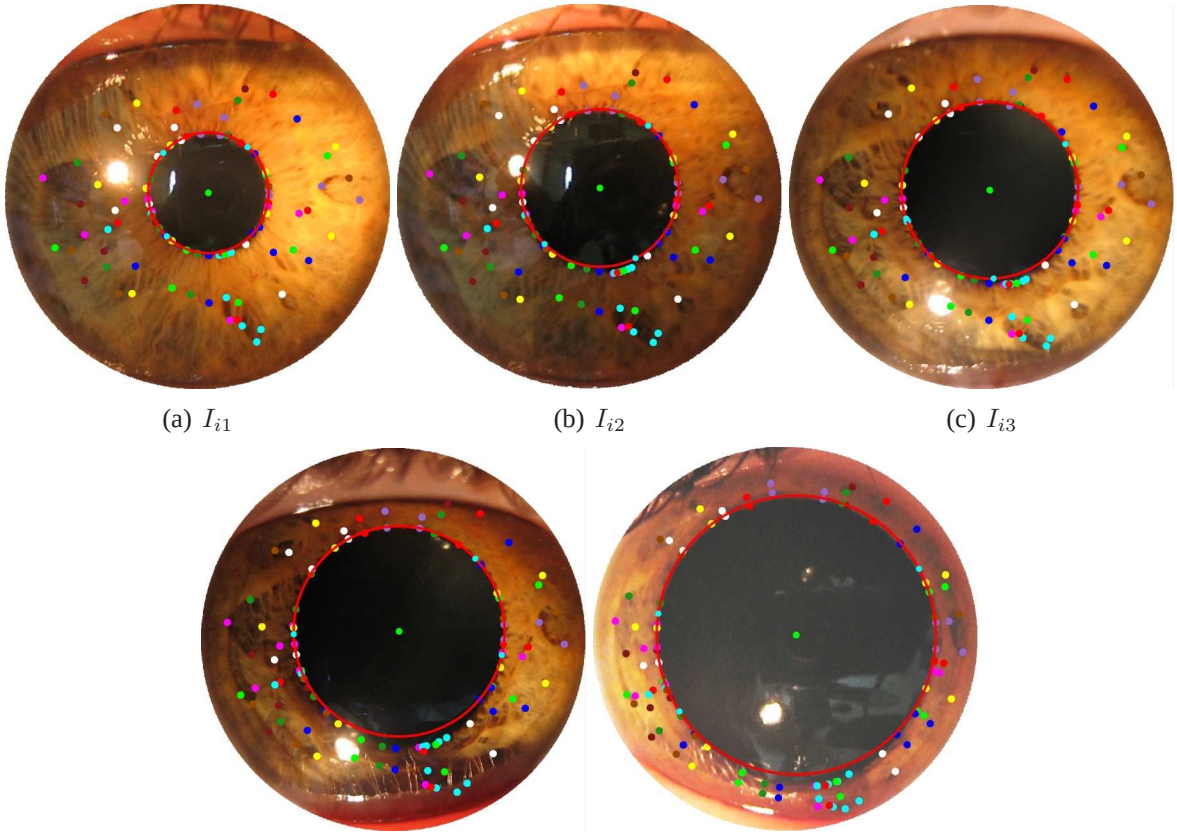

(a) I_{i1} (b) I_{i2} (c) I_{i3}

(d) I_{i4} (e) I_{i5}

Figure 6.4: Set of images used to track the 50 iridal features of one volunteer along the dilation process. Color dots indicate corresponding points in the different images $\{F_{i1k}...F_{i5k}\}$. From left to right, the pupil diameter values are: 3.70, 4.94, 5.53, 6.57, and 8.81 mm, respectively. The apparent changes in iris color are due to the changes in the position of the light source used to illuminate the subject's eye (the camera's flash was turned off).

(red circle), and the actual pupil border position B_{ijk} associated to each feature F_{ijk}. The complete set images used for tracking the features of the iris of this volunteer is shown in Figure 6.4. Figures 6.9 and 6.10 show some of the feature tracked points along the dilation process for two different subjects. In those examples a small number of points was used to facilitate the visual tracking of these points by the reader.

Figure 6.2 (right) shows how the positions of the individually tracked iridal feature points (identified by different colors) changed along the dilation process. The trajectories of the points both on the pupillary and ciliary zones move on approximately radial paths. Although some imprecision in the exact location of the points might have resulted from the manual specification, most of the deviation from the radial paths result from the existence of blood vessels under the iris, and from crypts, and folds (the iris folds its tissue as a result of pupil dilation) (Figure 6.7) that prevent iris points from always moving along radial lines. Such structures vary considerably among individuals but, their influence on the paths of the feature points usually have small magnitude (Figure 6.2 right). Therefore, as a first approximation, one can assume that the iris points move along straight lines in the radial directions. It is worth noting that Wyatt's 2D model (WYATT, 2000) does not take the influence of these structures into account either. Likewise, points on the pupil-

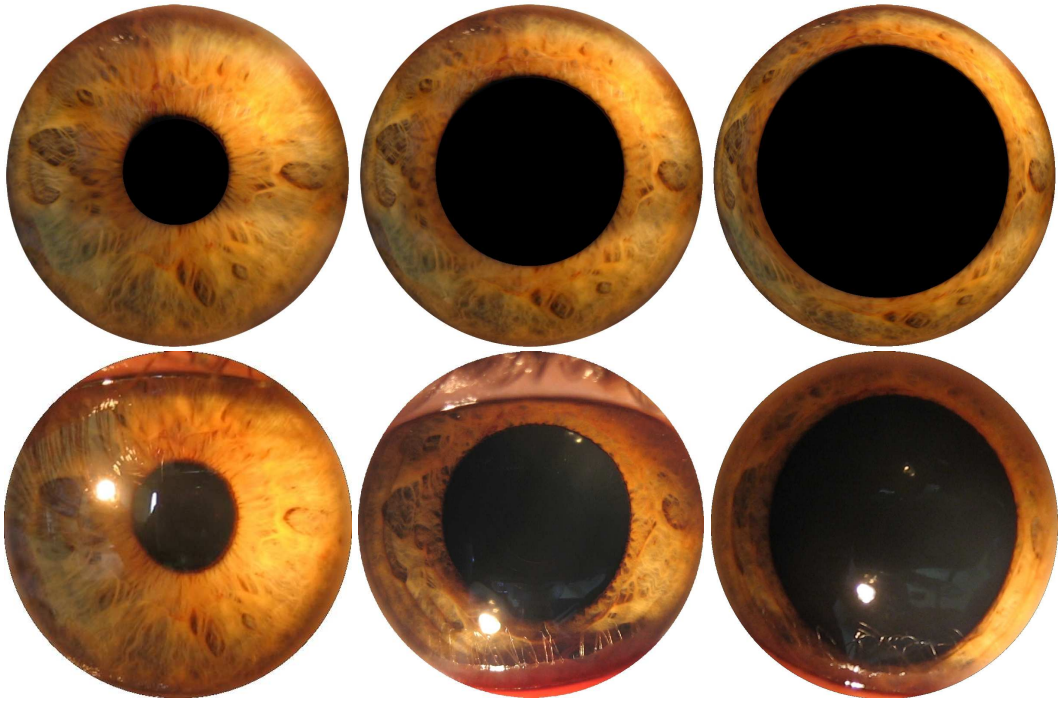

Figure 6.5: Comparison of the results produced by the proposed models with a set of photographs taken from the first subject. Top: renderings produced using the proposed models for environments illuminated with $35,638.70$ and $2,928.78$ lumens/mm^2, respectively, for the first two images. The third one simulates a mydriatic-induced dilation, a excessive pupil dilation due the use of mydriatic drops, such as tropicamide. No lighting model was used to render these images. Bottom: photographs of a human iris with the pupil at different diameters. The rightmost image was obtained after a mydriactic-induced dilation.

lary and ciliary zones also move in the same way (along radial lines), characterizing their movement as independent of muscle orientation.

In order to find how fast the feature points F_{ijk} moved, the following measures were computed during the dilation process: (i) the distance from the tracked feature point to the pupil center; (ii) the distance from the tracked feature point to the pupil border; and (iii) the ratio between the distance from the tracked point to the pupil border and the local width of the iridal disk. One should recall that the pupil is not necessarily circular and that its center does not necessarily coincide with the center of the iris. While measurements (i) and (ii) presented a pretty much linear behavior, the ratio represented by (iii) was approximately constant for all feature points (Figure 6.4 right). The same behavior was observed in the irises of all five volunteers. Like the variations in the trajectories of the points shown in Figure 6.2 (right), the deviations from horizontal lines in Figure 6.4 (right) are caused by the subjects' iris structures, specially the iridal folds. Again, as a first approximation, the following ratio can be assumed constant for any iridal point O_{ijk}, for all values of pupil diameters:

$$r_i = \frac{\|F_{ijk} - B_{ijk}\|}{\|O_{ijk} - B_{ijk}\|} \tag{6.1}$$

where O_{ijk} is a point on the iris outer circle collinear to the segment $F_{ijk} - B_{ijk}$ and $\|.\|$ is the l^2 norm. Then, the following invariance holds for feature point F_{ijk} for all values

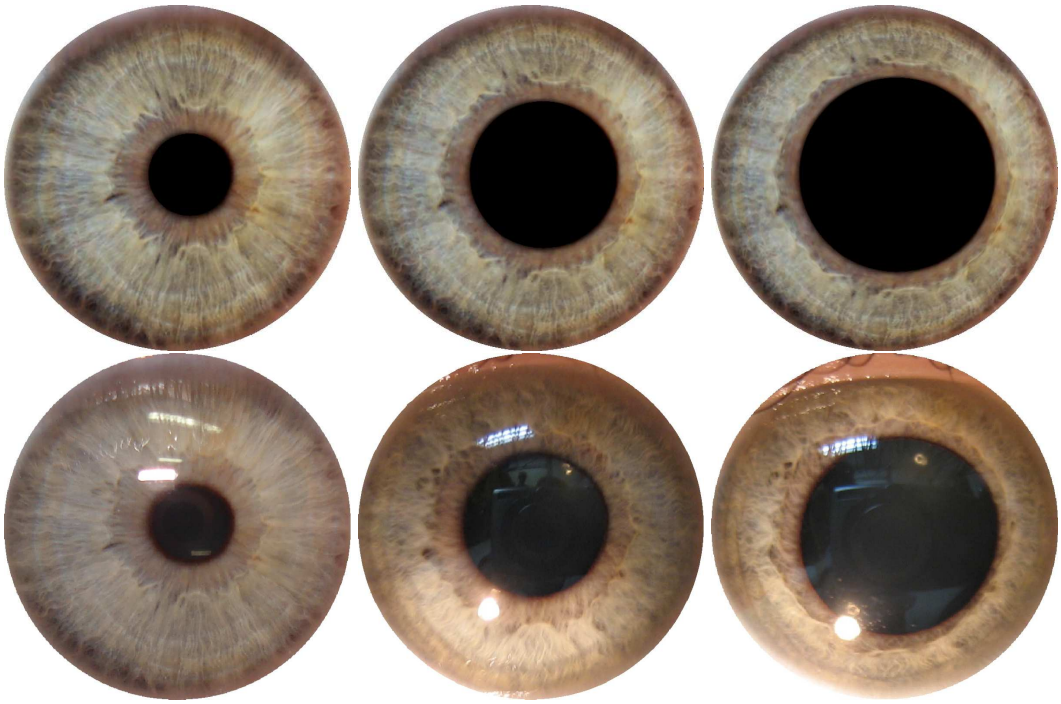

Figure 6.6: Comparison of the results produced by the proposed models with a set of photographs taken from a second subject. Top: renderings produced using the proposed models for environments illuminated with $373,304.70$ and $2,255$ lumens/mm^2, respectively, for the first two images. The third one simulates a mydriatic-induced dilation. No lighting model was used to render these images. Bottom: photographs of a human iris with the pupil at different diameters.

of pupil diameter. These measurements are plotted in the graphs shown in Figure 6.3. Figure 6.11 shows a comparison between the ratio r_i when the pupil is approximated by a perfect circle (top row) and when Equation 6.1 is used (middle row) for eight group of features.

Discounting the error introduced by the manual specification of the feature points and a little variance made by the influence of certain folds and blood vessels, one can assume the distances defined by (i) and (ii) vary linearly (Figures 6.3a and 6.3b, respectively), while the ratio in (iii) remains constant along the entire dilation process. Figures 6.12 and 6.13 show the graphs discussed in this section for two other volunteers. Figures 6.5 and 6.6 compares the results produced by the proposed models with real photographs. Note that the deformed patterns closely approximate the ones in the photographs.

Using high-resolution images of the human iris, crypts, pigment spots, and the collarette tend to move in a similar way. Such movements seem to be somehow independent of muscle influences, as suggested by Newsome and Loewenfeld (NEWSOME; LOEWENFELD, 1971). For all these structures, however, radial trajectories with minor deviations were observed at some points due to the existence of blood vessels and folds in the subject iris. Newsome and Loewenfeld did not comment this non-radial trajectories.

Some tracked features presents a non-linear behavior, as proposed by Rohen (1951) and formalized in a 2D model by Wyatt (2000). However, in this work, this do not always happens and the variations driven by blood vessels and folds are greater than that non-linearity 6.7. Thus, to consider the Wyatt's model and predict the behavior of a specific iris, it is needed first a 3D model for predict the influence of the blood vessels and folds in

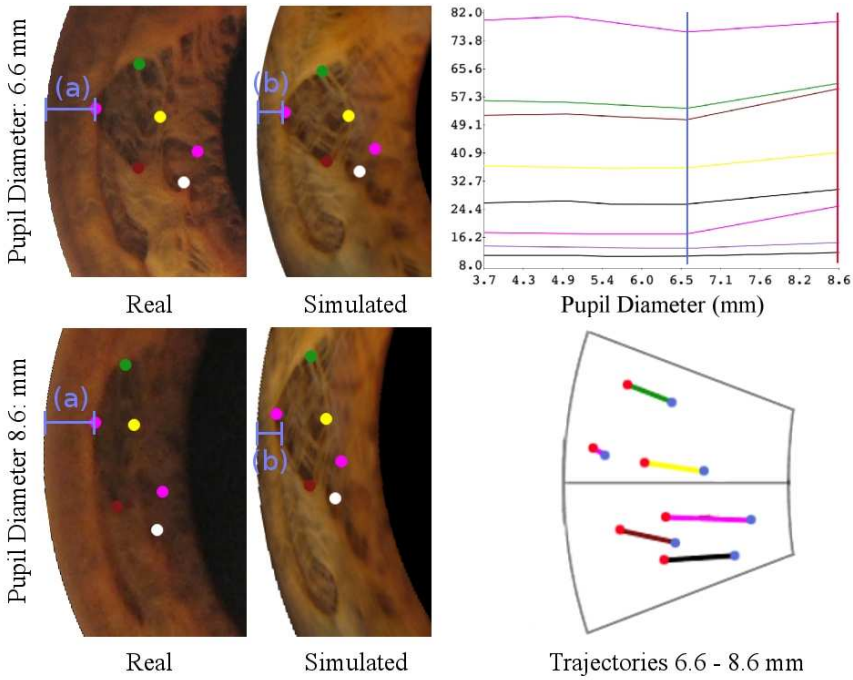

Figure 6.7: Example of the influence of folds in the radial trajectories and in the ratio. Left: real and simulated irises with pupil diameter of $6.6mm$ (top) and $8.6mm$ (bottom); right-top: the ratio r_i for each tracked feature as a function of pupil diameter; right-bottom: the trajectories of the tracked features from $6.6mm$ and $8.6mm$ of pupil diameter; (a) and (b) are the distance from pupil border to the feature in real and simulated irises. Although the (a) remains constant from $6.6mm$ to $8.6mm$, the (b) decreases folowing the image-based model.

the iris meshwork. Meanwhile, the approximation to radial trajectories and the constant ratio r_i creates a plausible animation of the iris.

6.1 Animating the Deformed Iridal Patterns

The animation of iridal pattern deformation was using a planar triangle-strip mesh on the disk defined by the two circles delimiting the iris (Figure 6.8 bottom) and using a picture of an iris with a small pupil diameter as a texture. Texture coordinates map the border of the pupil to the inner circle of the mesh, and outer border of the iris to the outer circle of the mesh. Currently, the mesh is tessellated creating a pair of triangles at every five degrees. The animation proceeds by computing the new pupil diameter D as a function of the incident lighting using Equation 5.10. Each vertex v_i, located on the inner circle of the mesh, is repositioned at a distance $D/2$ along the radial line connecting the center of the pupil to v_i, while keeping their original texture coordinates.

One should recall that the center of the pupil does not necessarily match the center of the iris, thus, it is important to keep the coordinates of the center of the pupil. When the pupil grows, you may also add a variation to the location at the in pupil center up to 20% to the nasal side (FREDDO, 1996).

Figure 6.8(top) shows two renderings created using the proposed model for pupil dilation/constriction and iridal pattern deformation. Note that the patterns deform in a very natural way. These images were simulated for light intensities of 10^5 Blondels (left) and

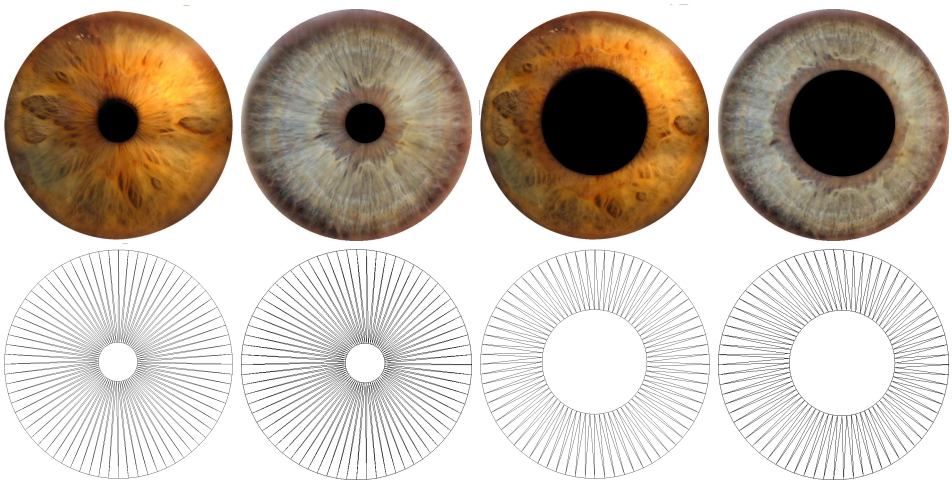

Figure 6.8: Example of irises rendered using the proposed model for pupil dilation/constriction and iridal pattern deformation. Note the natural deformation of the patterns. Top: images simulated for light intensities of 10^5 Blondels (left) and 1 Blondel (right). Bottom: triangle meshes used for renderings.

1 Blondel (right). The corresponding meshes are shown at the bottom.

Since the implementation of the proposed model uses texture mapping on planar triangle strips, and recalling that François *et al.* (2008) uses a height map to build a 3D mesh of the iris, one can extend the triangle strip by adding the height map to it, whose rendering allows, in close up views, the perception of shadows. Relief information could be added to the proposed model in a straightforward way, allowing some interesting shading effects such as projected shadows and self-occlusions (POLICARPO; OLIVEIRA; COMBA, 2005; OLIVEIRA; POLICARPO, 2005). This can avoid the distortion of the shadows or light as happens in Figure 6.6 (top). With a three dimensional model for the iris, other extension may support the Lam and Baranoski model (LAM; BARANOSKI, 2006), creating a realistic and predictable iris synthesis and animation. Also, no corneal refraction is used. Thus, at grazing angles, in addition to the distortion resulting from pupil dilation/constriction, one would perceive the projective distortion due to texture mapping.

6.2 Summary

This chapter presented an image-based model for iridal pattern deformation. The images generated by the proposed model were compared with photographs taken during light and drug pupil-induced dilation. It also suggested some possibilities for future work supporting the ILIT model (LAM; BARANOSKI, 2006) and the François *et al.* (2008) 3D rendering technique.

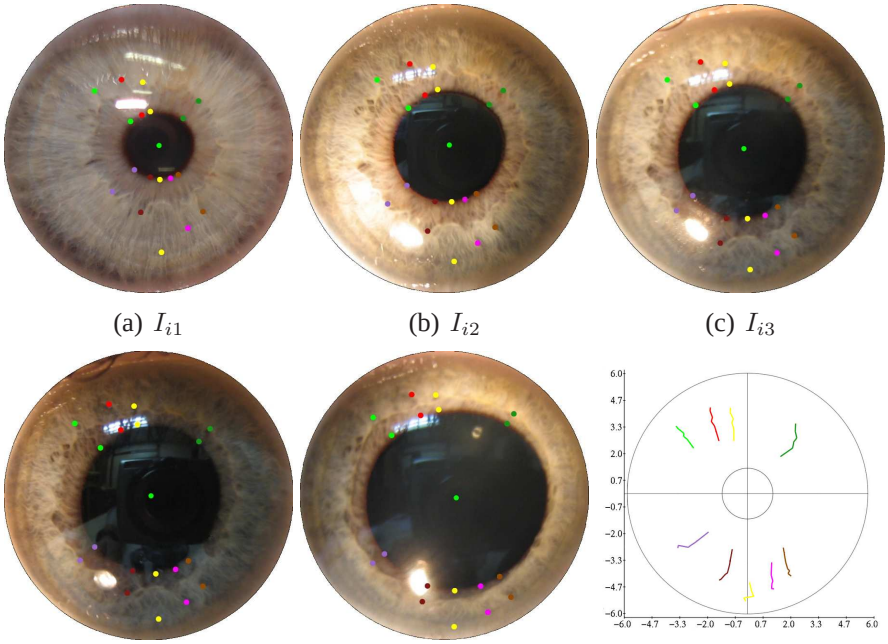

(a) I_{i1} (b) I_{i2} (c) I_{i3}

(d) I_{i4} (e) I_{i5} (f)

Figure 6.9: A subset of the 22 feature points from subject number two tracked along the dilation process: (a) to (e). A plot of the trajectory of these points (f)

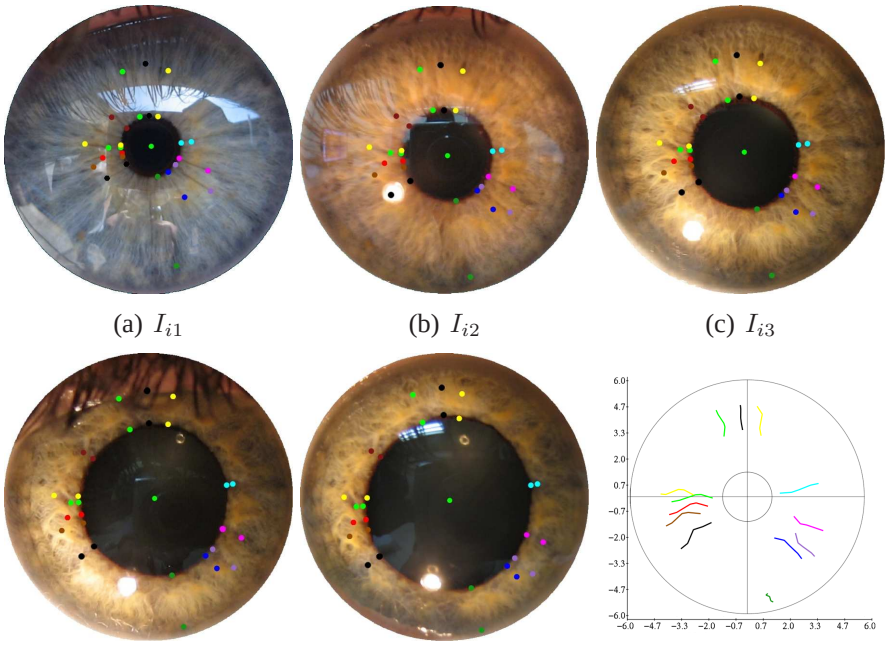

(a) I_{i1} (b) I_{i2} (c) I_{i3}

(d) I_{i4} (e) I_{i5} (f)

Figure 6.10: A subset of the 29 feature points from subject number two tracked along the dilation process: (a) to (e). A plot of the trajectory of these points (f)

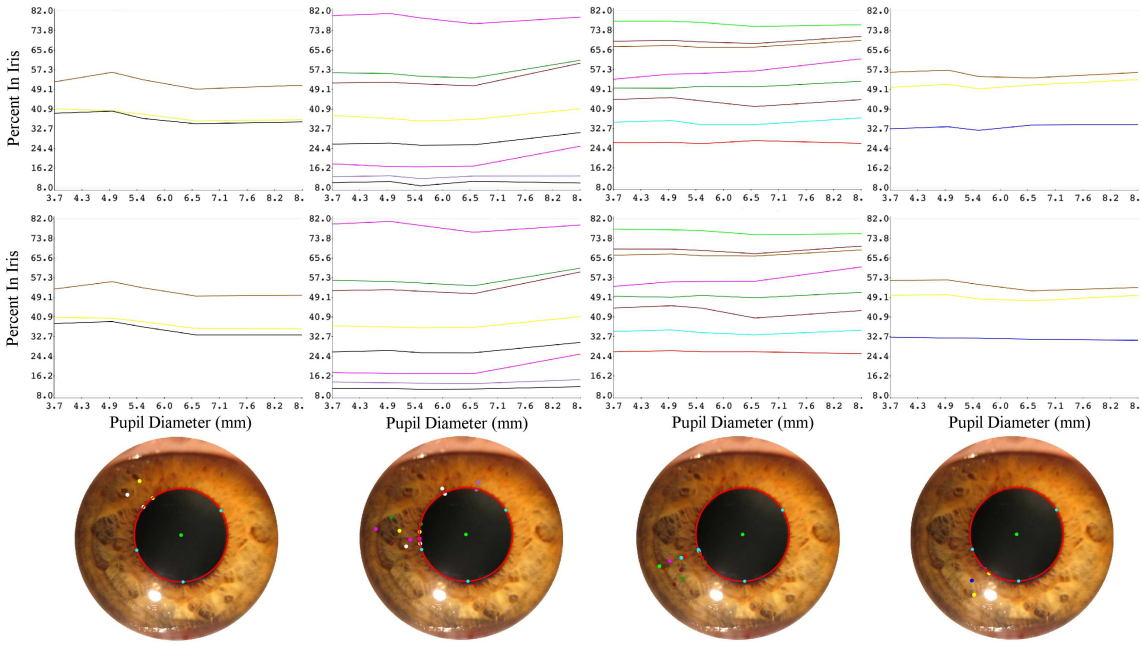

(a) Groups: 1-4

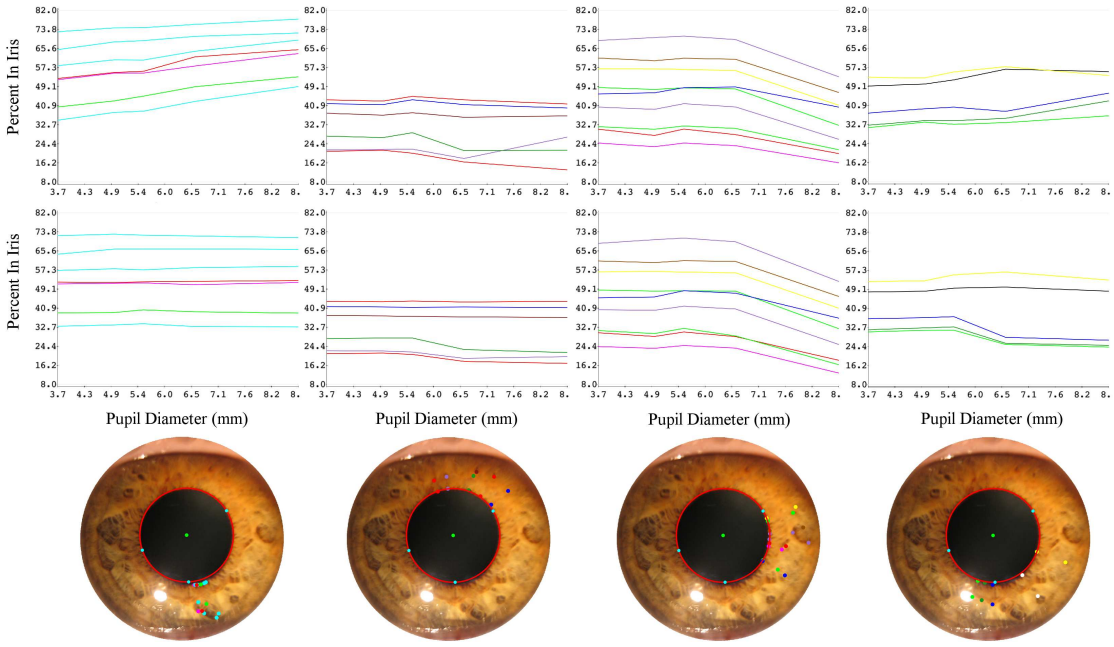

(b) Groups: 5-8

Figure 6.11: The 50 feature points showed in Figure 6.2 divided in eight groups. The top rows of (a) and (b) show the evolution of the ratio between the distance from the feature point to the pupil border, defined by the red circle, and the local width of the iridal disk. The middle rows of (a) and (b) show the same ratio but with the pupil border defined by B_{ijk}. The bottom images show the group of points considered in each column.

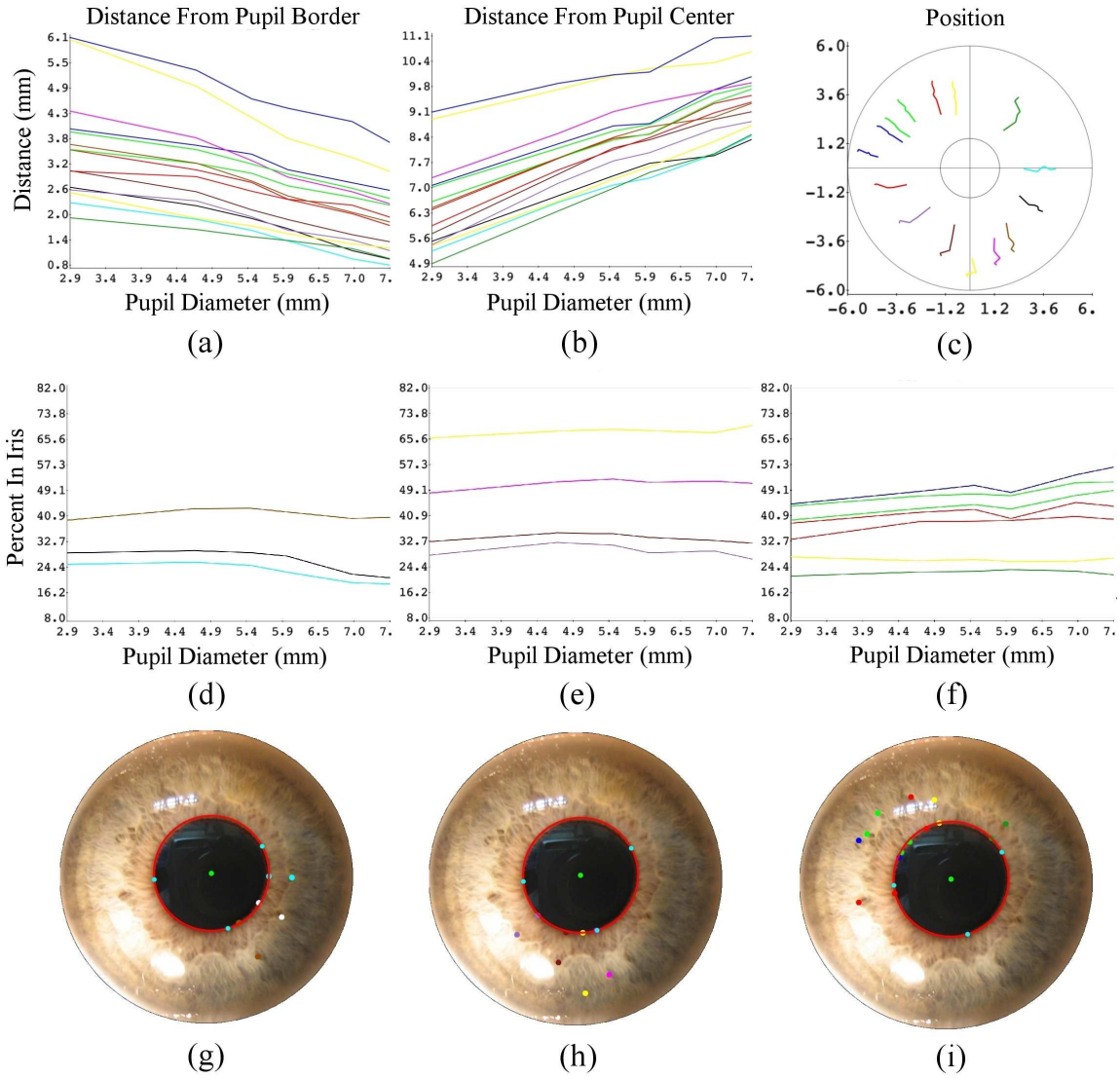

Figure 6.12: Result of the tracked feature points for a second subject. (a) and (b) show the position of each feature F_{ijk} relative to pupil center and pupil border respectively. Note the linearity of these graphs. (c) the trajectories of each feature point when the pupil dilates. (d), (e) and (f) are the ratio r_i (Equation 6.1). Note that, despite some precision problems when marking the features, these ratios are approximately constant.

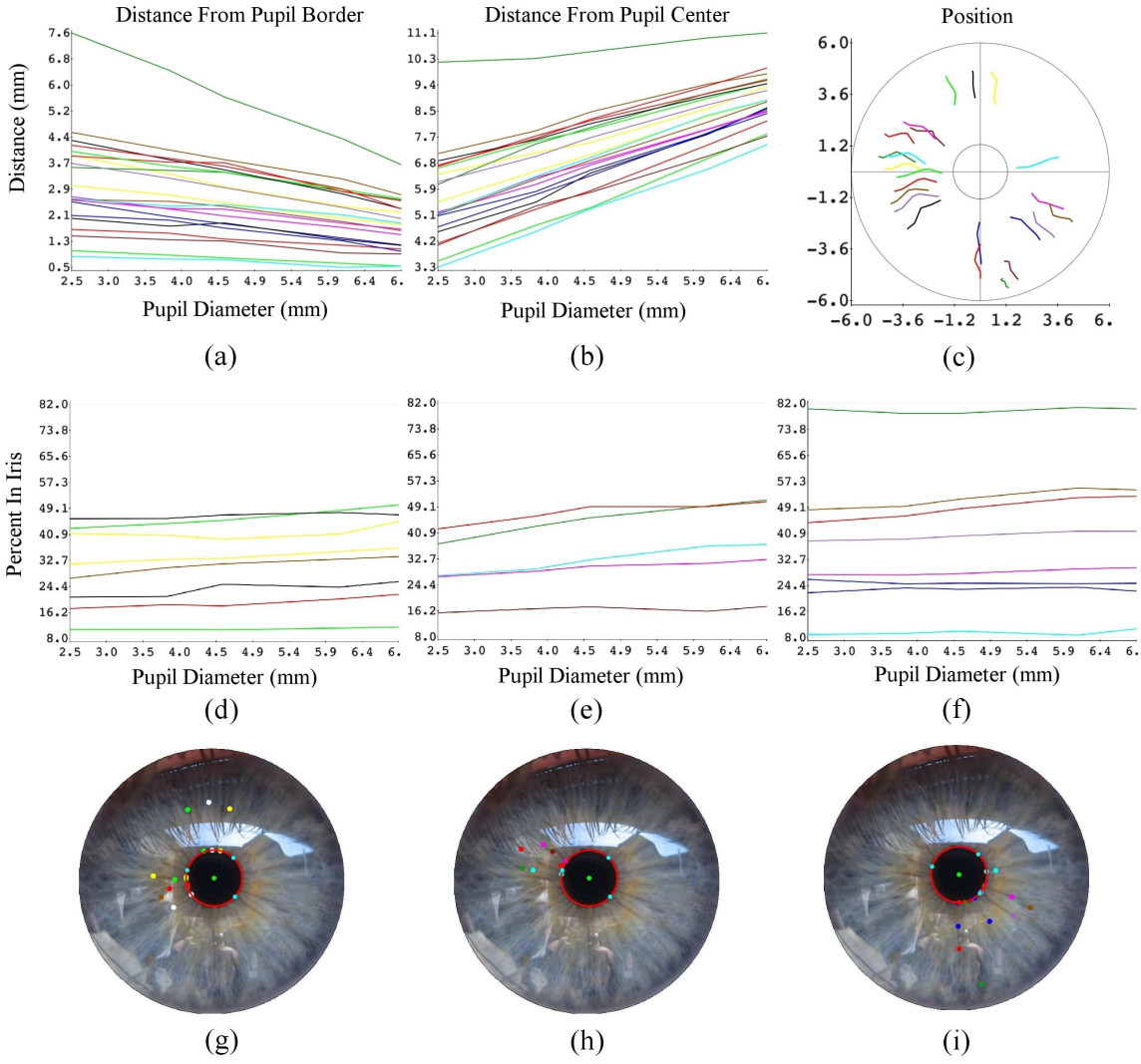

Figure 6.13: Result of the tracked feature points for a third subject. (a) and (b) show the position of each feature F_{ijk} relative to pupil center and pupil border respectively. Note the linearity of these graphs. (c) the trajectories of each feature point when the pupil dilates. (d), (e) and (f) are the ratio r_i (Equation 6.1). Note that, despite some precision problems when marking the features, these ratios are approximately constant.

7 APPLICATION OF THE PROPOSED MODELS IN COMPUTER GRAPHICS

In order to demonstrate the potential use of the proposed models in computer graphics, this thesis presents an application example, which renders a human head model in an environment illuminated by high dynamic range (HDR) light probes. A light probe image is an omnidirectional image that records the incident illumination for each solid angle[1]. An HDR light probe image is a light probe that allows a greater range of exposures than normal digital imaging techniques. The intention of HDR is to accurately represent the wide range of intensity levels found in real scenes recording an scaled value in $lumens/mm^2$. The HDR images were obtained from Paul Debevec's web site (DEBEVEC, 2007) and from ICT Graphics Lab (INSTITUTE OF CREATIVE TECHNOLOGIES, 2007).

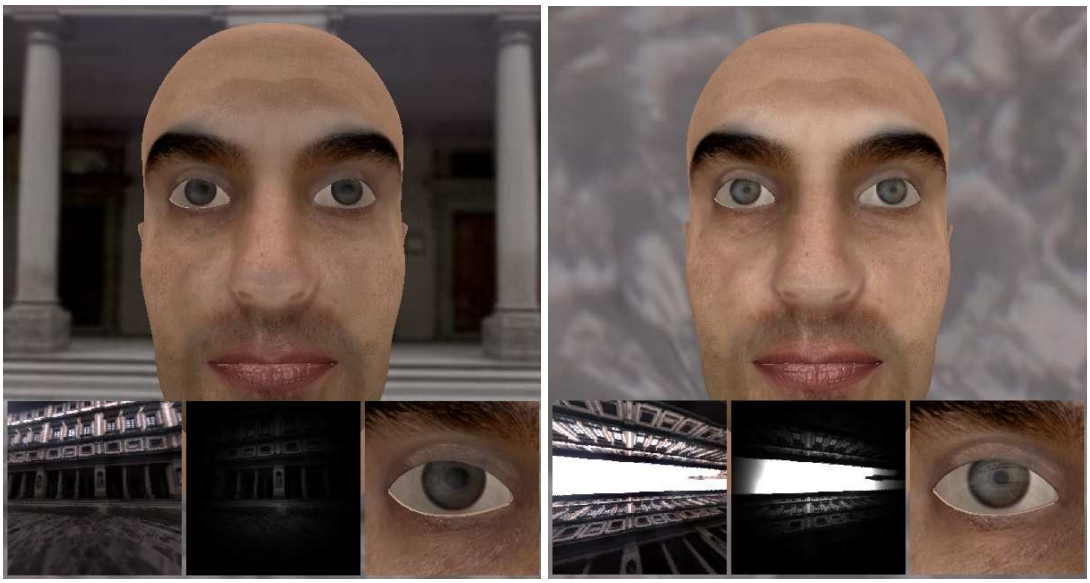

Figure 7.1: Two screenshots from the demo application created to illustrate the use of the proposed models in computer graphics. From left to right, the small images at the bottom show, respectively: the part of the environment seen by the model; an approximation to the image perception on the retina; and a close-up of the eye. Note the differences when looking to a darker place (the building in the left screenshot) and looking to the bright sky (right screenshot).

The head models were obtained from freely available repositories on the net (TURBO

[1]The 3D counterpart of the 2D angle, *i.e.*, formed by the radial projection of an object onto a unit sphere instead of unit circle (GLASSNER, 1995)

SQUID, 2007; BLENDER ARTISTS, 2007) and its original irises were replaced by the textured triangle-strip as needed by the proposed model. As the head looks at different parts of the environment, its pupil diameters adapt to the irradiance in the solid angle defined by its field of view. This produces interesting animation effects.

Figure 7.1 shows two screenshots of this application. The head model looks at different directions: to the building (Figure 7.1 left) and to the sky (Figure 7.1 right). The small images at the bottom, show, from left to right: (i) the portions of the environment seen by the model; (ii) an approximation to the image perception on the retina and (iii) a close-up view of the model's eyes. Since the distribution of rods and cones in the human retina can be seen as a Gaussian density function with the center at the fovea (HADJIKHANI; TOOTELL, 2000; JONAS; SCHNEIDER; NAUMANN, 1992), in this application, the perceived luminance is approximated by modulating the projection of the environment seen by the model (small image at the bottom center of Figure 7.1) using a three-standard-deviation Gaussian filter and summing the luminance of all pixels. Note the changes in pupil size between the two images. The iris on the left was rendered as a perfectly diffuse surface. The rendering on the right includes some Fresnel effect to partially reflect the environment on the cornea surface. Normal maps[2], specular maps[3] and ambient occlusion (BUNNELL, 2005) were also applied to the face. Ambient occlusion is a global shading method that approximates the full global illumination, identifying for each vertex a shadow coefficient. The Lamb skin effect (nVidia, 2007) was implemented to improve the realism of the skin, since it provides a computationally efficient way to visually approximate subsurface light scattering effects (Figure 7.2).

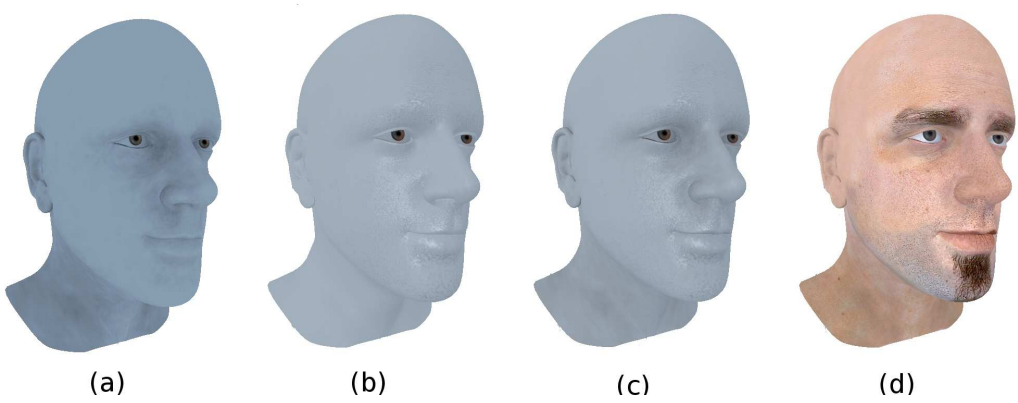

Figure 7.2: Main effects included in the application to produce realistic renderings. (a) Ambient occlusion (BUNNELL, 2005); (b) Lamb skin effect (nVidia, 2007); (c) Lamb skin eEffect plus ambient occlusion; (d) Final rendering with texture and specular maps.

Unfortunately, the HDR images do not contain the scenes actual luminance values, they are scaled. Thus, in order to produce plausible pupil and iris animations, the stored values are divided by 100.0 and treated the resulting value as lumens per square millimeter. In the future, one can capture HDR images with luminance values in the right scale. This would allow us to compare the animations to real footage obtained in the scene.

[2]Normal maps define the normals of a set of discrete points on a surface.
[3]Specular maps record the specular intensity and color of highlights on a surface.

7.1 Summary

This chapter presented an application illustrating the use of the two proposed models to render a 3D model of a human face. An HDR light probe and the models simulate the iridal response to perceived luminance. Many effects were included to produce a more realistic rendering of a human face.

8 CONCLUSION AND FUTURE WORK

This thesis presented new models for realistic renderings of the human iris and pupil light reflex. The proposed physiologically-based model of the pupil light reflex first combines theoretical results from the Mathematical Biology field (LONGTIN; MILTON, 1989) with experimental data collected by several researchers (MOON; SPENCER, 1944), using latency and velocity models from the biological literature. The simplest version of the model is expressed in terms of a non-linear delay-differential equation that describes the changes in the pupil diameter as a function of the environment lighting. As all parameters of the proposed model were derived from experimental data, they correctly represent the actual behavior of the human iris and pupil from an average subject.

Due to the large variability among individuals, this basic version of the model was extended to include differences, which are modelling as isocurves bounded by the biggest and smallest pupil diameter values found in the original data used by Moon and Spencer (MOON; SPENCER, 1944), along the entire range of luminance values. In order to improve the realism of the resulting simulations, hippus effect is approximate by adding small random variations to the environment light (in the range of 0.05Hz to 0.3Hz (STARK, 1939)). The complete model was evaluated by comparing the pupil diameters predicted by the model to measurements made on iris video sequences (on a frame by frame basis), in tree different experiments, for two individuals exhibiting different degrees of light sensitivity.

Other contribution of this work is a study of the iridal pattern deformation as a function of pupil dilation and constriction, as well as an image-based model for realistic animation of such deformations. After an analysis of many high-resolution pictures taken from four volunteers with different induced pupil sizes during an induced pupil-dilation process, the ratio expressed by Equation 6.1 was kept approximately constant for all points on iris, and for all tested subjects, independent of the pupil diameter. For rendering purposes, the model of the iris was built as a planar triangle-strip mesh on the disk defined by the two circles delimiting the iris and using a picture of an iris with a small pupil diameter as a texture. The animation moves the mesh points of the pupil border, increasing or decreasing the pupil radius.

An application that renders a human head model in an environment illuminated by HDR light probes was built in order to demonstrate the potential use of the proposed models in computer graphics. As the head looks at different parts of the environment, its pupil diameters adapt to the irradiance in the solid angle defined by its field of view, producing pleasing animation effects. The proposed models guided by biophysical meaningful parameters produce high-fidelity appearance effects and can be used to produce real-time, predictive and reproducible animations of the pupil and iris under variable lighting conditions and individual differences.

To the best of our knowledge, the proposed PLR model is the first physiologically-based model for simulating pupil light reflex presented in the graphics literature. It is also the first practical model (*i.e.*, providing actual parameter values) in the literature for simulating the dynamics of pupil and iris under variable lighting conditions, and the first integrated model in all literature to consider individual variability in pupil diameter using general equations for latency, velocity, and an approximation to hippus effect. The proposed image-based model for iridal pattern deformation is the first model of its kind in the graphics literature. The results should find immediate applicability in several areas requiring high-fidelity facial animations, as well as on feature film animations, where the request for increasing levels of realism never ends.

We believe that this work can also contribute to investigations outside the scope of computer graphics. More specifically, the simulation tools presented in this paper can be used to complement wet experiments and accelerate the hypothesis evaluation cycle in ophthalmological and physiological research. It is worth mentioning that computer simulations are being successfully and routinely used by biologists and medical researchers to study the predictive behavior of living systems under various conditions, including some not yet experimentally tested (VENTURA et al., 2006).

8.1 Discussions and Future Work

For future work, the proposed model could be improved to consider the influence of accommodation and emotional conditions in pupil size. Accommodation and age affect the pupil diameter (WINN et al., 1994) and iris color influences some PLR parameters, such as maximum pupil diameter, latency, and constriction velocity (BERGAMIN et al., 1998). These aspects are currently not taken into account by the proposed model. The main reason is the lack of reliable data over a large range of lighting conditions. For instance, Winn *et al.* (1994) discuss the effect of age on the size of the pupil. Their study, however, only considered luminance values from 10^1 to 10^4 Blondels, which corresponds to only about 30% of the luminance range used by the proposed model. Currently, variations in pupil diameters for the same light stimulus were modeled using Equation 5.10, which can approximate the age-related miosis effect reported by Winn *et al.*. Extending the proposed model to handle other phenomena based on biophysical parameters is an interesting direction for future work.

Since, the proposed PLR model was created assuming some uniform light-intensity distribution, it does not consider the light position relative to the viewer. An extension of the model can consider the light position, predicting the Stiles-Crawford effect (*i.e.* the phenomenon that light reaching the retina after passing near the edge of the pupil is less effective at evoking sensation than light passing through the center of the pupil (STILES; CRAWFORD, 1933)) and observing the distribution of rods and cones in the human retina (HADJIKHANI; TOOTELL, 2000).

HDR light probes record the incident illumination for each solid angle. However, using the representation as proposed by Debevec et al. (2002), it is not possible to retrieve the true luminance value in $lumens/mm^2$ as needed by the PLR model. Thus, a new type of light probe can be defined that stores luminous flux (measured in lumens), which could be used for physically accurate simulations and renditions of PLR using the proposed model.

The current implementation of the proposed iris deformation model uses texture mapping on a planar triangle strip. Such a model can be extended with a height map in a way

similar to the technique described in (FRANÇOIS et al., 2008). The rendering of this new model will include support to self-shadowing and view-motion parallax, noticeable in closeup views. Other extension may support the Lam and Baranoski (2006) model, creating a realistic and predictable iris synthesis and animation.

The Longtin and Milton's model and, by inheritance, the proposed PLR model, predicts a small and fast oscillation in pupil diameter when the pupil dilates using the pupil latency as a function of light intensity. This behavior was not documented in the literature and the digital video sequences has no sufficient accuracy to show this oscillation. Some work will be necessary to verify the actually occurrence of such a predicted behavior. Such a study should probably require the use of specialized equipment, and can be used either to validate this prediction or, otherwise, provide valuable feeback to refine the latency model proposed by Link and Stark (1988) and Ellis (1981) and used as part of the PLR model.

The irises of animals have the same functionality of the human ones. An interesting work could be a validation or adaptation of the iris deformation model against monkeys (CLARKE; ZHANG; GAMLIN, 2003a,b; MAGOUN et al., 1936), cats (HAMMOND; MOUAT, 1985; SCHAEPPI; KOELLA, 1964; MITCHELL, 2006), rabbits (YAMAJI et al., 2003), pigeons (PILAR; VAUGHAN, 1971) or other animals (WEST et al., 1991). This thesis can be used as a guideline to create PLR and iris deformation models for other species.

REFERENCES

BARANOSKI, G. V. G.; LAM, M. W. Y. Qualitative assessment of undetectable melanin distribution in lightly pigmented irides. **Journal of Biomedical Optics**, [S.l.], v.12, n.3, p.030501–1 – 030501–3, May/June 2007.

BELL, A. L. **Histology lab IX**: the eye. Available at: <http://faculty.une.edu/com/abell/histo/histolab3b.htm>. Visited on: Nov. 21, 2007.

BERG, T. J. T. P. V. D.; TAN, K. E. W. P. Light transmittance of the human cornea from 320 to 700 nm for different ages. **Vision Research**, [S.l.], v.34, p.1453–1456, June 1994.

BERGAMIN, O. et al. The influence of iris color on the pupillary light reflex. **Graefes Arch. Clin. Exp. Ophthalmol.**, [S.l.], v.236, n.8, p.567–570, 1998.

BERGAMIN, O.; ZIMMERMAN, M. B.; KARDON, R. H. Pupil light reflex in normal and diseased eyes: diagnosis of visual dysfunction using waveform partitioning. **Ophthalmology**, [S.l.], v.110, n.1, p.106–114, 2003.

BLENDER ARTISTS. **Broken Shadows**: portrait, grunge theme. Available at: <http://blenderartists.org/forum/showthread.php?t=103053>. Visited on: Nov. 21, 2007.

BOETTNER, E. A.; WOLTER, J. R. Transmission of the Ocular Media. **IOVS**, [S.l.], v.1, p.776–783, 1962.

BORES, L. D. **Ocular Anatomy**. Available at: <http://e-sunbear.com/>. Visited on: Nov. 21, 2007.

BUNNELL, M. Dynamic Ambient Occlusion and Indirect Lighting. **GPU Gems 2 - Programming Techniques for High-Performance Graphics and General-Purpose Computation**. [S.l.]: Addison Wesley, 2005. p.223–234.

CALCAGNINI, G. et al. Spontaneous fluctuations of human pupil reflect central autonomic rhythms. **Methods Inf. Med.**, [S.l.], v.39, n.2, p.142–145, June 2000.

CLARKE, R. J.; ZHANG, H.; GAMLIN, P. D. R. Primate Pupillary Light Reflex: receptive field characteristics of pretectal luminance neurons. **J. Neurophysiol.**, [S.l.], v.89, p.3168–3178, 2003.

CLARKE, R. J.; ZHANG, H.; GAMLIN, P. D. R. Characteristics of the Pupillary Light Reflex in the Alert Rhesus Monkey. **J. Neurophysiol.**, [S.l.], v.89, p.3179–3189, 2003.

CRAWFORD, B. H. The integration of the glare effects from a number of glare sources. **Proc. Phys. Soc.**, [S.l.], v.48, n.1, p.35–37, Jan. 1936.

CUI, J. et al. An Iris Image Synthesis Method Based on PCA and Super-Resolution. In: INTERNATIONAL CONFERENCE ON PATTERN RECOGNITION, 2004. **Proceedings...** Washington: IEEE Computer Society, 2004. v.4, p.471–474.

DAUGMAN, J. How Iris Recognition Works. In: INTERNATIONAL CONFERENCE ON IMAGE PROCESSING, 2002. **Proceedings...** [S.l.: s.n.], 2002. p.21–30.

DEBEVEC, P. Image-Based Lighting. **IEEE Computer Graphics and Applications**, Los Alamitos, v.22, n.2, p.26–34, Mar./Apr. 2002.

DEBEVEC, P. **Paul Debevec Home Page**. Available at: <http://www.debevec.org/>. Visited on: Nov. 21, 2007.

DECKERT, C. **Eye Design Book**. Available at: <http://www.eyedesignbook.com/index.html>. Visited on: Nov. 21, 2007.

ELLIS, C. J. The pupillary light reflex in normal subjects. **British Journal of Ophthalmology**, [S.l.], v.65, n.11, p.754–759, Nov. 1981.

ESCALOFRIO.FREE.FR. **Fondos de Escritorio Escalofriantes**. Available at: <http://escalofrio.free.fr/fon_orcos/>. Visited on: Nov. 21, 2007.

FERWERDA, J. A. Three Varieties of Realism in Computer Graphics. **Proceedings of SPIE - The International Society for Optical Engineering**, Bellingham, Washington, n.5007, p.290–297, June 2003.

FRANÇOIS, G. et al. Anatomically accurate modeling and rendering of the human eye. In: ACM SIGGRAPH, 2007. **Proceedings...** New York: ACM, 2007. p.59.

FRANÇOIS, G. et al. Subsurface Texture Mapping. **IEEE Computer Graphics and Applications**, Los Alamitos, CA, v.28, n.1, p.34–42, Jan./Feb. 2008.

FREDDO, T. Ultrastructure of the Iris. **Microscopy Research and Technique**, [S.l.], v.33, p.369–389, 1996.

GLASSNER, A. **Principles of Digital Image Synthesis**. San Francisco: Morgan Kaufmann, 1995.

GLOBO. **Wallpaper Eva Byte**. Available at: <http://www.red-pixel.com.br/images/news/wallpapereva.jpg>. Visited on: Nov. 21, 2007.

GROOT, S. G. de; GEBHARD, J. W. Pupil size as determined by adapting luminance. **J. Opt. Soc. Am.**, [S.l.], v.42, p.492–495, 1952.

GUILLOUZIC, S.; HEUREUX, I. L.; LONGTIN, A. Small delay approximation of stochastic delay differential equations. **Physical Review E**, [S.l.], v.59, n.4, p.3970–3982, 1999.

HACHOL, A. et al. Measurement of pupil reactivity using fast pupillometry. **Physiol. Meas.**, [S.l.], v.28, p.61–72, 2007.

HADJIKHANI, N.; TOOTELL, R. B. H. Projection of rods and cones within human visual cortex. **Human Brain Mapping**, [S.l.], v.1, n.9, p.55–63, 2000.

HAMMOND, P.; MOUAT, G. S. V. The relationship between feline pupil size and luminance. **Experimental Brain Research**, [S.l.], v.59, n.3, p.485–490, 1985.

HESS, E. H.; POLT, J. M. Pupil size in relation to mental activity during simple problem-solving. **Science**, [S.l.], v.143, p.1190–1192, Mar. 1964.

HILL, A. V. The heat of shortening and the dynamic constants of muscle. **Proc. R. Soc. London B. Biol. Sci.**, [S.l.], v.126, p.136–195, 1938.

HOT WHEELS. **Acceleracers**. Available at: <http://www.hotwheels.com/acceleracers/index.aspx>. Visited on: Nov. 21, 2007.

IMESCH, P.; WALLOW, I.; ALBERT, D. The color of the human eye: a review of morphologic correlates and of some conditions that affect iridial pigmentation. **Surv. Ophthalmol.**, [S.l.], v.41, Suppl. 2, p.177, Feb. 1997.

INSTITUTE OF CREATIVE TECHNOLOGIES. **ICT Graphics Lab**. Available at: <http://gl.ict.usc.edu/>. Visited on: Nov. 21, 2007.

JCH DIGITAL DESIGNS. **Give Your Characters Life**. Available at: <http://www.cocs.com/poser/bestrender2.htm>. Visited on: Nov. 21, 2007.

JONAS, J. B.; SCHNEIDER, U.; NAUMANN, G. O. H. Count and density of human retinal photoreceptors. **Graefe's Archive for Clinical and Experimental Ophthalmology**, [S.l.], v.230, n.6, p.505–510, Oct. 1992.

KASTHURIRANGAN, S.; GLASSER, A. Characteristics of pupil responses during fat-to-near and near-to-far accommodation. **Ophthal. Physiol. Opt.**, [S.l.], v.25, p.328–339, 2005.

KOJIMA, M. et al. Pupillary light reflex in panic disorder. A trial using audiovisual stimulation. **Eur. Arch. Psychiatry Clin. Neurosci.**, [S.l.], v.254, n.4, p.242–244, 2004.

KRENZ, W. et al. Neurophysiological model of the normal and abnormal human pupil. **IEEE Transactions on Biomedical Engineering**, [S.l.], v.BME-32, n.10, p.817–825, 1985.

LAM, M. W. Y.; BARANOSKI, G. V. G. A Predictive Light Transport Model for the Human Iris. **Computer Graphics Forum**, [S.l.], v.25, n.3, p.359–368, 2006.

LEE, S.; BADLER, J.; BADLER, N. Eyes Alive. **ACM Transactions on Graphics**, [S.l.], v.21, n.3, p.637–644, 2002.

LEFOHN, A. et al. An Ocularist's Approach to Human Iris Synthesis. **IEEE Comput. Graph. Appl.**, Los Alamitos, CA, USA, v.23, n.6, p.70–75, 2003.

LI, Z.; LIANG, P.; SUN, F. Properties of pupillary responses to dynamic random-dot stereograms. **Exp. Brain Res.**, [S.l.], v.168, p.436–440, 2006.

LI, Z.; SUN, F. Pupillary response induced by stereoscopic stimuli. **Exp. Brain Res.**, [S.l.], v.160, p.394–397, 2005.

LINK, N.; STARK, L. Latency of the pupillary response. **IEEE Trans. Bio. Eng.**, [S.l.], v.35, n.3, p.214–218, 1988.

LONGTIN, A.; MILTON, J. G. Modelling autonomous oscilations in the human pupil light reflex using non-linear delay-differential equations. **Bulletin of Math. Bio.**, [S.l.], v.51, n.5, p.605– 624, 1989.

LOWENSTEIN, O.; LOEWENFELD, I. E. The sleep-waking cycle and pupillary activity. **NYAS Annals**, [S.l.], v.117, p.142–156, 1964.

MAGOUN, H. W. et al. The afferent path of the pupillary light reflex in the monkey. **Brain**, [S.l.], v.59, p.234–249, 1936.

MAKTHAL, S.; ROSS, A. Synthesis of Iris Images using Markov Random Fields. In: EUROPEAN SIGNAL PROCESSING CONFERENCE, 2005, Antalya, Turkey. **Proceedings...** [S.l.: s.n.], 2005.

MITCHELL, N. Feline ophthalmology Part 1: examination of the eye. **Irish Veterinary Journal**, [S.l.], v.59, n.3, p.164–168, 2006.

MMVII New Line Productions. **The Lord Of The Rings**. Available at: <http://www.lordoftherings.net/legend/gallery/>. Visited on: Nov. 21, 2007.

MOON, P.; SPENCER, D. On the Stiles-Crawford Effect. **J. Opt. Soc. Am.**, [S.l.], v.34, p.319–329, 1944.

NEWSOME, D.; LOEWENFELD, I. Iris mechanics. I. Influence of pupil size on dynamics of pupillary movements. **Am. J. Ophthalmol.**, [S.l.], v.71, n.1 Part 2, p.347–362, Jan. 1971.

NICODEMUS, F. E. et al. **Geometrical considerations and nomenclature for reflectance**. [S.l.]: Final Report National Bureau of Standards, Washington, DC. Inst. for Basic Standards., 1977.

NORBURY, J.; WILSON, R. E. Dynamics of Constrained Differential Delay Equations. **J. Comput. Appl. Math**, [S.l.], v.125, p.201–215, 2000.

nVidia. **Lamb Skin Dusk Effect**. Available at: <http://http.download.nvidia.com/developer/SDK/Individual_Samples/effects.html>. Visited on: Nov. 21, 2007.

nVidia nZone. **NVIDIA Demo: adrianne**. Available at: <http://www.nzone.com/object/nzone_adrianne_home.html>. Visited on: Nov. 21, 2007.

OHTA, N.; ROBERTSON, A. **Colorimetry**: fundamentals and applications. Chichester, England: John Wiley & Sons, 2005. p.1–38.

OLIVEIRA, M. M.; POLICARPO, F. **An Efficient Representation for Surface Details**. Porto Alegre, Brazil: UFRGS, 2005. (RP-351).

PARTRIDGE, L. D.; BENTON, L. A. Muscle: the motor. BROOKS, V. B. **Handbook of Physiology**. Washington: American Physiological Society, 1981. v.2, p.43–106.

PAUL, C. A. H. Developing a delay differential equation solver. **Appl. Numer. Math.**, Amsterdam, The Netherlands, v.9, n.3, p.403–414, 1992.

PEASE, A.; PEASE, B. **The Definitive Book of Body Language**. Rio de Janeiro, RJ, Brasil: Bantam, 2004. v.1, p.103–124.

PILAR, G.; VAUGHAN, P. C. Ultrastructure and Contractures of the Pigeon Iris Striated Muscle. **Journal of Physiology**, [S.l.], v.219, p.253–266, March 1971.

PINGNET, B. et al. Feedback in action: the mechanism of the iris. **Phys. Educ.**, [S.l.], v.23, p.31–35, 1988.

PIXAR. **The Incredibles**. Available at: <http://www.pixar.com/featurefilms/incredibles/>. Visited on: Nov. 21, 2007.

PIXAR. **Finding Nemo**. Available at: <http://www.pixar.com/featurefilms/nemo/>. Visited on: Nov. 21, 2007.

POKORNY, J.; SMITH, V. C. How much light reaches the retina? In: SYMPOSIUM OF THE INTERNATIONAL RESEARCH GROUP ON COLOUR VISION DEFICIENCIES, 13., 1995, Pav, France. **Color Vision Deficiencies XIII**: proceedings. Dordrecht: Kluwer Academic, 1995. p. 491-511.

POLICARPO, F.; OLIVEIRA, M. M.; COMBA, J. L. D. Real-time relief mapping on arbitrary polygonal surfaces. In: I3D '05: PROCEEDINGS OF THE 2005 SYMPOSIUM ON INTERACTIVE 3D GRAPHICS AND GAMES, 2005, New York, NY, USA. **...** ACM, 2005. p.155–162.

PRIVITERA, C. M.; STARK, L. W. A Binocular Pupil Model for Simulation of Relative Afferent Pupil Defects and the Swinging Flashlight Test. **Bio. Cyber.**, [S.l.], v.94, p.215–224, 2006.

PROENÇA, H. P. M. C. **Towards Non-Cooperative Biometric Iris Recognition.** 2006. Tese (Doutorado em Ciência da Computação) — University of Beira Interior.

REBELANCER. **Rebelance ShrekTW**. Available at: <http://www.rebelancer.com/2005/rebelance_shrektw.jpg>. Visited on: Nov. 21, 2007.

REEVES, P. The response of the average pupil to various intensities of light. **J. Opt. Soc. Am.**, [S.l.], v.4, n.2, p.35–43, Mar. 1920.

ROHEN. Der bau der Regenbogenhaut beim Menschen und einigen Säugern. **Gegenbaur Morphology Journal**, [S.l.], v.91, p.140–181, 1951.

SAGAR, M. et al. A virtual environment and model of the eye for surgical simulation. In: SIGGRAPH CONFERENCE, 1994, Orlando. **Computer Graphics**: proceedings. New York: ACM, 1994. p. 205-213.

SCHACHAR, R. A. Growth patterns of fresh human crystalline lenses measured by in vitro photographic biometry. **Journal of Anatomy**, [S.l.], v.206, p.575, June 2005.

SCHAEPPI, U.; KOELLA, W. P. Innervation of cat iris dilator. **Am. J. Physiol.**, [S.l.], v.207, p.1411–1416, 1964.

SCHMID, R. et al. Effect of Age on the Pupillomotor Field. **Clinical Neural Ophthalmology**, [S.l.], v.24, n.3, p.228–234, Sept. 2004.

SCHOR, C. M.; BHARADWAJ, S. R. A pulse-step model of accommodation dynamics in the aging eye. **Vision Res.**, [S.l.], v.45, n.10, p.1237–1254, May 2005.

SfondiDelDesktop.com. **Images Toon**: a bug s life. Available at: <http://www.sfondideldesktop.com/Images-Toon/A-Bug-S-Life/>. Visited on: Nov. 21, 2007.

STARK, L. W. Stability, Oscillations, and Noise in the Human Pupil Servomechanism. **Proc. of the IRE**, [S.l.], v.47, n.11, p.1925–1939, 1939.

STARK, L. W.; SHERMAN, P. M. A servoanalytic study of consensual pupil reflex to light. **J. Neurophysiol.**, [S.l.], v.20, p.17–26, 1959.

STILES, W. S.; CRAWFORD, B. H. The luminous efficiency of rays entering the eye pupil at different points. **Proc. Roy Soc.**, [S.l.], v.B112, p.428, 1933.

STRAUB, R. H.; THIES, U.; KERP, L. The pupillary light reflex. 1. Age-dependent and age-independent parameters in normal subjects. **Ophthalmologica**, [S.l.], v.204, n.3, p.134–142, 1992.

SULEIMAN, M. B.; ISLMAIL, F. Solving delay differential equations using componentwise partitioning by Runge-Kutta method. **App. Math. and Comp.**, [S.l.], v.122, n.3, p.301–323, 2001.

TAMM, S.; TAMM, E.; ROHEN, J. W. Age-related changes of the human ciliary muscle: a quantitative morphometric study. **Mech. Ageing Dev.**, [S.l.], v.62, n.2, p.209–221, Feb. 1992.

THOMSON, L. C. Binocular summation within the nervous pathways of the PLR. **J. Physiology**, [S.l.], v.106, p.59–65, 1947.

TILMANT, C. et al. Monitoring and modeling of pupillary dynamics. In: ANNUAL INTERNATIONAL CONFERENCE OF IEEE ON ENGINEERING IN MEDICINE AND BIOLOGY SOCIETY, 25., 2003, Cancún, Mexico. **Proceedings...** Piscataway: NJ: IEEE, 2003. v.1, p.678–681.

TREVOR-ROPER, P. D.; CURRAN, P. V. The Eyeball. **The Eye and Its Disorders**. Oxford, Boston: Blackwell Scientific Publications; St. Louis, Mo.: Distributors, USA, Blackwell Mosby, 1984. v.3, p.3–75.

TURBO SQUID. **3D max male face head**. Available at: <http://www.turbosquid.com/FullPreview/Index.cfm/ID/357993>. Visited on: Nov. 21, 2007.

TWENTIETH CENTURY FOX. **Ice Age**: the meltdown. Available at: <http://www.iceagemovie.com/>. Visited on: Nov. 21, 2007.

UKAI, K. Spatial pattern as a stimulus to the pupillary system. **J. Opt. Soc. Am. A**, [S.l.], v.2, n.7, p.1094–1100, July 1985.

UKAI, K.; TSUCHIYA, K.; ISHIKAWA, S. Induced pupillary hippus following near vision: increased occurrence in visual display unit workers. **Ergonomics**, [S.l.], v.40, n.11, p.1201–1211, Nov. 1997.

USUI, S.; STARK., L. A model for nonlinear stochastic behavior of the pupil. **Biological Cybernetics**, [S.l.], v.45, n.1, p.13–21, Aug. 1982.

VENTURA, B. et al. From *in vivo* to *in silico* biology and back. **Nature**, [S.l.], v.443, p.527–533, 2006.

WATT, A.; WATT, M. **Advanced Animation and Rendering Techniques**. New York: Addison-Wesley, 1992.

WECKER, L.; SAMAVATI, F.; GAVRILOVA, M. Iris Synthesis: a reverse subdivision application. In: COMPUTER GRAPHICS AND INTERACTIVE TECHNIQUES IN AUSTRALASIA AND SOUTH EAST ASIA, 2005, Dunedin, New Zealand. **Proceedings...** New York: ACM, 2005. v.1, p.121–125.

WEI, Z.; TAN, T.; SUN, Z. Nonlinear Iris Deformation Correction Based on Gaussian Model. In: INTERNATIONAL CONFERENCE ON ADVANCES IN BIOMETRICS, ICB, 2007, Soul, Korea. **Advances in Biometrics**: proceedings. Berlin: Springer, 2007. p. 780-789. (Lecture Notes in Computer Science, v. 4642).

WERNER, A. Spectral sensitivity of the pupillary system. **Clin. Exp. Optom.**, [S.l.], v.86, n.4, p.235–238, 2003.

WEST, J. A. et al. A comparative study of the anatomy of the iris and ciliary body in aquatic mammals. **Can. J. Zool.**, [S.l.], v.69, n.10, p.2594–2607, 1991.

WIKIPEDIA: the free encyclopedia. **Eye**. Available at: <`http://en.wikipedia.org/wiki/Eye`>. Visited on: Nov. 21, 2007.

WINN, B. et al. Factors Affecting Light-Adapted Pupil Size in Normal Human Subjects. **IOVS**, [S.l.], v.35, n.3, Mar. 1994.

WYATT, H. J. A minimum-wear-and-tear meshwork for the iris. **Vision Research**, [S.l.], v.40, p.2167–2176, 2000.

WYATT, H. J. Particular conversation about his meshwork for the iris at Nov. 21, 2007 by e-mail: <wyatt@sunyopt.edu>.

YAMAJI, K. et al. Mechanical properties of the rabbit iris smooth muscles. **Vision Res.**, [S.l.], v.43, n.4, p.479–487, Feb. 2003.

YOSHIDA, H. et al. Time-varying properties of respiratory fluctuations in pupil diameter of human eyes. **Methods Inf. Med.**, [S.l.], v.33, n.1, p.46–48, Mar. 1994.

YOSHIDA, H. et al. Statistical properties of simultaneously recorded fluctuations in pupil diameter and heart rate. In: IEEE EMBS, 1995, Montreal. **Proceedings...** Washington: IEEE Computer Society, 1995. v.1, p.165–166.

YUAN, X.; SHI, P. A Non-linear Normalization Model for Iris Recognition. In: INTERNATIONAL WORKSHOP ON BIOMETRIC RECOGNITION SYSTEMS, IWBRS, 2005 Beijing, China. **Advances in Biometric Person Authentication**: proceedings. Berlin: Springer, 2005. (Lecture Notes in Computer Science, v. 3781).

ZUO, J.; SCHMID, N. A. A Model Based, Anatomy Based Method for Synthesizing Iris Images. In: INTERNATIONAL CONFERENCE ON ADVANCES IN BIOMETRICS, ICB, 2006, Hong Kong, China. **Advances in Biometrics**: proceedings. Berlin: Springer, Jan. 2006. p. 428-435. (Lecture Notes in Computer Science, v. 3832).

ZUO, J.; SCHMID, N. A.; CHEN, X. On Performance Comparison of Real and Synthetic Iris Images. In: ICIP, 2006. **Proceedings...** [S.l.: s.n.], 2006. p.305–308.

APPENDIX A UNIT CONVERSION TABLE

Table A.1 shows values used to perform unit conversions among the radiometric and photometric quantities employed in this thesis.

Table A.1: Unit Conversion Table

Value-Unit	.Value	Unit
1.00 candela/square m. [cd/m^2]	3.141592654	Blondel
	0.314159265	millilambert [mL]
	0.291863508	foot-Lambert [fL]
1.00 Blondel	0.1	millilambert [mL]
	0.09290304	foot-Lambert [fL]
1.00 millilambert [mL]	0.9290304	foot-Lambert [fL]
1.00 lux [lx]	1.00	lumen/square m. [lm/m^2]
1.00 watt/square centimeter [a]	683.00×10^4	lumen/square m. [lm/m^2]
1.00 Blondel [b]	10.00×10^{-6}	lumens/square mm. [lm/mm^2]

[a] With a light bulb emitting light at 555 nm

[b] Assuming a perfect diffuse (Lambertian) reflector (OHTA; ROBERTSON, 2005)

APPENDIX B MODELOS FOTOREALISTAS PARA O REFLEXO PUPILAR À LUZ E DEFORMAÇÃO DOS PADRÕES DA ÍRIS

Resumo da Dissertação em Português

Animar faces humanas virtuais consiste em imitar uma realidade cheia de detalhes e comum aos nossos olhos. Grande parte da expressão de um personagem é dado por movimentos oculares e pelas variações pupilares: contração e dilatação. São estes movimentos que, se realizados de forma coerente, prendem a atenção dos espectadores e transmitem o sentimento desejado pelo autor (LEE; BADLER; BADLER, 2002; WATT; WATT, 1992).

Diferente do resto do corpo, o olho humano e a pupila respondem a estímulos involuntários, que são determinados pelas condições de iluminação, estado emocional e distância focal, entre outras (REEVES, 1920; ELLIS, 1981; CALCAGNINI et al., 2000). O reflexo pupilar à luz (Pupillary Light Reflex - PLR) é responsável pela contração da pupila em ambientes iluminados e por sua dilatação em ambientes escuros. PLR é uma ação reconhecida, comum aos nossos olhos, e, exceto pela influência de drogas, é o principal fator que determina o tamanho da pupila. Embora o PLR e as deformações da íris possam ser animadas utilizando técnicas tradicionais de computação gráfica como, por exemplo, representações paramétricas controladas por curvas de velocidade, nós acreditamos que o uso de modelos fisiológicos, guiados por parâmetros com significado físico, possam tornar o processo preditível e automático, criando animações realistas e reprodutíveis.

Neste trabalho nós apresentamos um modelo fisiológico para animação realista do reflexo pupilar a lux. Nosso modelo combina e estende modelos teóricos (LONGTIN; MILTON, 1989) com dados coletados por vários experimentos relacionando o diâmetro pupilar a intensidade de luz do ambiente (MOON; SPENCER, 1944). Como a íris humana é uma camada muscular fibro-vascular que define padrões que são deformados em função do tamanho da pupila, nós modelamos estas deformações baseando-se em uma análise do comportamento das estruturas visíveis da íris a partir de um conjunto de fotografias. Estas fotografias foram obtidas durante um processo de dilatação induzida das pupilas de vários voluntários..

Pelo que pesquisamos, nosso modelo fisiológico para PLR é o primeiro da literatura de computação gráfica. É também o primeiro modelo capaz de simular variações individuais em termos de sensibilidade a luz e o primeiro modelo para deformação dos padrões da íris em toda a literatura. Nós demonstramos a eficácia da nossa abordagem comparando os resultados dos nossos modelos contra fotografias e vídeos capturados de iris humanas.

B.1 Modelos Existentes Para PLR

A pupilometria descreve modelos, construídos a partir de experimentos e um conjunto de medidas discretas, que relacionam diretamente a iluminação que atinge a retina com um tamanho médio da pupila de um conjunto de indivíduos (MOON; SPENCER, 1944; GROOT; GEBHARD, 1952; POKORNY; SMITH, 1995). As medidas são tomadas quando a pupila está estável, após a alteração da iluminação. Estes modelos são todos atemporais, portanto não descrevem o comportamento fora do estado de equilíbrio. De todos eles, o modelo mais popular é o de Moon e Spencer (MOON; SPENCER, 1944), que é dado por:

$$D = 4.9 - 3tanh\left[0.4(log_{10}(L_b) - 0.5)\right] \tag{B.1}$$

onde o diâmetro pupilar D varia de 2 a 8mm, e L_b é o nível de luminância do ambiente expressa em Blondels e variando de 10^5 Blondels em dias ensolarados até 10^{-5} Blondels em noites escuras.

Modelos para PLR, baseados em observações anatômicas e fisiológicas, foram criados para expressar o relacionamento entre as diversas estruturas do corpo humano envolvidas no processo, sem considerar dados experimentais. Longtin e Milton (1989) definiram um modelo teórico para o caminho neural entre o estímulo de luz recebido pela pupila até a ação de contração ou dilatação da íris:

$$\frac{dg}{dA}\frac{dA}{dt} + \alpha g(A) = \gamma\ ln\left[\frac{\phi(t-\tau)}{\bar{\phi}}\right] \tag{B.2}$$

onde

$$g(A) = \sqrt[n]{\frac{\Lambda\theta^n}{A - \Lambda'} - \theta^n} \tag{B.3}$$

e Λ' e $\Lambda + \Lambda'$ são respectivamente áreas mínima e máxima que a pupila pode assumir, θ é o valor para a atividade muscular quando a pupila possui tamanho médio, α e γ são fatores de proporcionalidade, t é o tempo, τ é a latência entre o momento do estímulo e a resposta da íris, ϕ é o nível de luz na retina medida em lumens e definido como $\phi = IA$, onde I é a iluminância em lumens/mm^2, A é a área da pupila em mm^2 e $\bar{\phi}$ é um limite inferior para o nível de luz no qual variações abaixo dele não provocam alteração na área pupilar), $g(A)$ representa uma função com um intervalo pré-definido no conjunto imagem e simula as propriedades elasto-mecânicas dos músculos em geral.

Note que, embora este modelo seja temporal, as constantes não representam unidades físicas. Por exemplo, θ é definido sobre uma unidade não conhecida e, portanto não pode ser medida, chamada atividade muscular. Valores incorretos para estas constantes podem criar comportamentos não realistas e não convergir para uma solução.

B.2 Proposta de modelo para PLR

Nosso modelo combina o modelo teórico e temporal de Longtin e Milton (Equation B.2) e o modelo experimental e estático de Moon e Spencer (Equation B.1).

Sob iluminação constante, a área pupilar no modelo de Longtin e Milton convergirá para um estado de equilíbrio, onde:

$$\frac{dg}{dA}\frac{dA}{dt} = 0$$

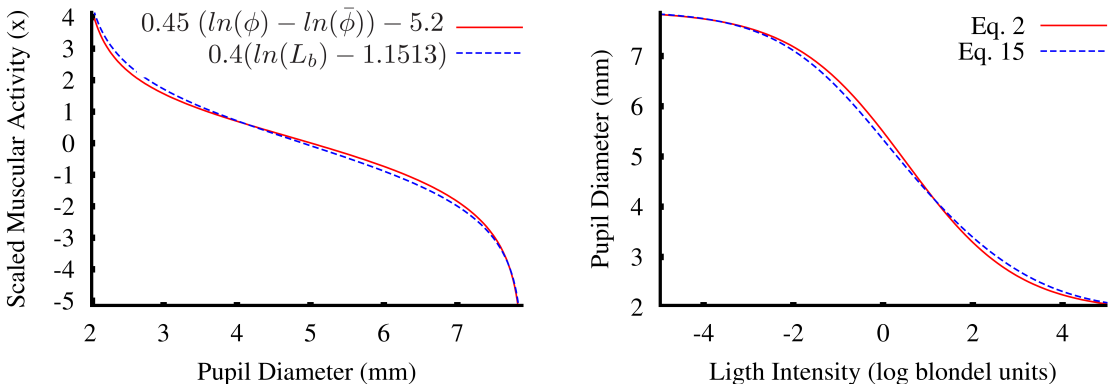

Figura B.1: Qualidade dos Fittings: (esquerda) Ambos os lados da equação B.8. (direita) Equações B.1 e B.10, na qual a diferença em valores absolutos é menor que 2% sob o intervalo $[10^{-5}, 10^{5}]$ Blondels.

Sob esta circunstância e assumindo que não há ocorrência de hippus[1], ϕ torna-se independente de tempo. Manipulando algebricamente os modelos, podemos reescrevê-los pelas equações abaixo:

$$\alpha g(A) = \gamma\ (ln(\phi) - ln(\bar{\phi})) \tag{B.4}$$

$$-2.3026\ atanh\left(\frac{D-4.9}{3}\right) = 0.4(ln(L_b) - 1.1513) \tag{B.5}$$

onde $atanh$ é o arco-tangente hiperbólico. Note a semelhança no formato das equações. Para que a Equação B.4 apresente valores de área pupilar comparáveis ao diâmetro pupilar utilizado na Equação B.5, sob as mesmas condições de iluminação, tem-se:

$$-2.3026\ atanh\left(\frac{D-4.9}{3}\right) \approx \alpha g(A) \tag{B.6}$$

$$0.4(ln(L_b) - 1.1513) \approx \gamma(ln(\phi) - ln(\bar{\phi})) \tag{B.7}$$

Ajustando-se as duas equações, obtém-se:

$$0.4(ln(L_b) - 1.1513) \approx 0.45\ (ln(\phi) - ln(4.8118\ \times\ 10^{-10})) - 5.2 \tag{B.8}$$

A figura Figura B.1(esquerda) mostra a qualidade da aproximação. Dada a Equação B.6, pode-se substituir $\alpha g(A)$ por $M(D)$ e utilizar os valores das constantes do lado esquerdo da Equação B.8 na Equação B.4. O modelo que prediz o diâmetro pupilar em condições de iluminação estável pode ser expresso como:

$$M(D) = atanh\left(\frac{D-4.9}{3}\right) \tag{B.9}$$

$$2.3026\ M(D) = 5.2 - 0.45\ ln\left[\frac{\phi}{4.8118\ \times\ 10^{-10}}\right] \tag{B.10}$$

[1]Hippus são pequenas variações orientadas pelo sistema nervoso autônomo geralmente refletindo o estado emocional do indivíduo.

Voltando a considerar o modelo temporal, podemos efetuar a mesma troca da função atemporal $g(a)$ pela $M(D)$ e utilizar os mesmos valores para as constantes. Desta forma, o nosso modelo dinâmico é a Equação B.11:

$$\frac{dM}{dD}\frac{dD}{dt} + 2.3026\ atanh\left(\frac{D-4.9}{3}\right) = 5.2 - 0.45\ ln\left[\frac{\phi(t-\tau)}{4.8118\ \times\ 10^{-10}}\right] \qquad \text{(B.11)}$$

onde D e ϕ são expressos em mm e $lumens$, respectivamente. Para latência τ, nós utilizamos o modelo de Link e Stark (1988).

Como velocidade de contração é aproximadamente três vezes mais rápida do que a velocidade de (re)dilatação (ELLIS, 1981; BERGAMIN et al., 1998), nós aplicamos esta diferença no tamanho do passo da simulação numérica que resolve o modelo:

$$dt_c = \frac{T_c - T_p}{S} \qquad dt_d = \frac{T_c - T_p}{3S} \qquad \text{(B.12)}$$

one dt_c e dt_d são medidos em millisegundos, T_c e T_p são, respectivamente, os tempo de simulação atual e anterior medido em millisegundos. S é uma constante que afeta as velocidades no sentido de simular variações individuais.

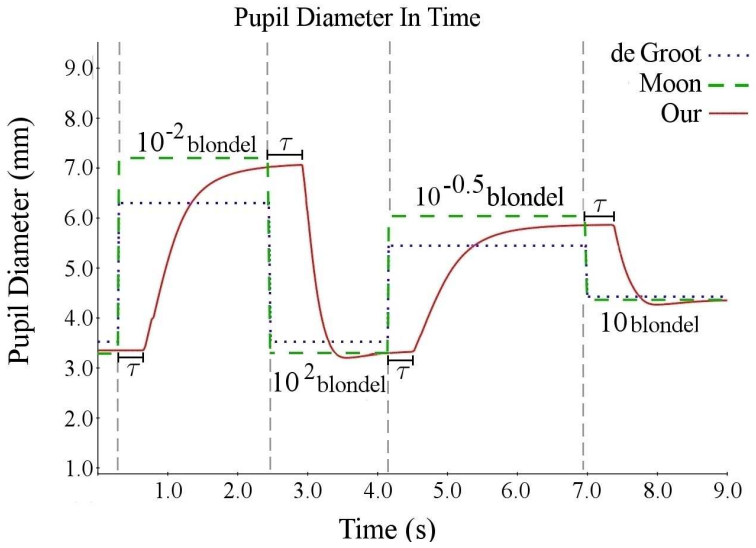

Figura B.2: Resultados da simulação utilizando nosso modelo (linha sólida) (Equação B.11) para o indivíduo médio de Moon e Spencer sobre condições de iluminação variáveis. Estes resultados são comparados com os modelos estáticos de Moon e Spencer (1944) (linha tracejada), e de Groot e Gebhard (1952) (linha pontilhada). Note a latência em nosso modelo.

Figura B.2 mostra a evolução do diâmetro pupilar para um indivíduo médio de Moon e Spencer. O Gráfico compara a Equação B.11 com a Equação B.1. Os nossos resultados também são comparados contra o modelo de Groot e Gebhard.

Embora que a Equação B.11 simule o comportamento de um indivíduo médio representando pela curva de Moon e Spencer, existem variações entre indivíduos relacionadas aos seguintes parâmetros: latência (CRAWFORD, 1936; MOON; SPENCER, 1944; GROOT; GEBHARD, 1952; ELLIS, 1981) e velocidade de contração e (re)dilatação (ELLIS, 1981; BERGAMIN et al., 1998). Para estimar estas diferenças individuais nós criamos um intervalo de variação dado por curvas de diâmetro pupilar máximo e mínimo

baseado nos dados de Moon e Spencer, como mostrado na Figura B.3. A partir desta informação, cria-se iso-curvas C_I entre os limites máximo e mínimo. O diâmetro pupilar final é definido resolvendo a Equação 5.8 e utilizando o diâmetro encontrado na equação B.13

$$D_{final} = C_b(D) + (C_t(D) - C_b(D))r_I \tag{B.13}$$

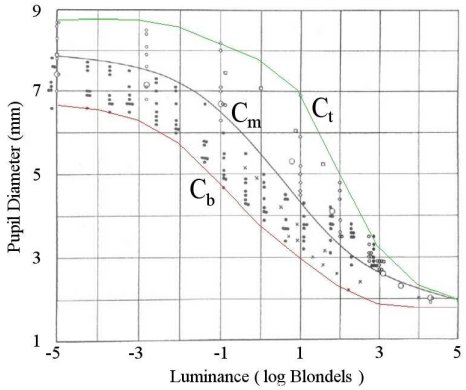

Figura B.3: Dados originais de Moon e Spencer (1944). A curva C_m corresponde a Equação 5.7. O par de curvas C_b e C_t definem um envelope contendo a faixa de diâmetro pupilar disponível para cada intensidade de luz.

Para aproximar a hippus, pequenas variações pupilares que ocorrem mesmo com uma intensidade de luz estável, adiciona-se pequenas variações na intensidade de luz na faixa de $10^{-0.5}$ e $10^{0.5}$ Blondels e na freqüência de 0.05Hz a 0.3Hz (STARK, 1939). Estas variações melhoram consideravelmente o realismo das animações. Validamos a aproximação junto com o novo modelo comparando com dados reais, como mostrado na Figura B.4.

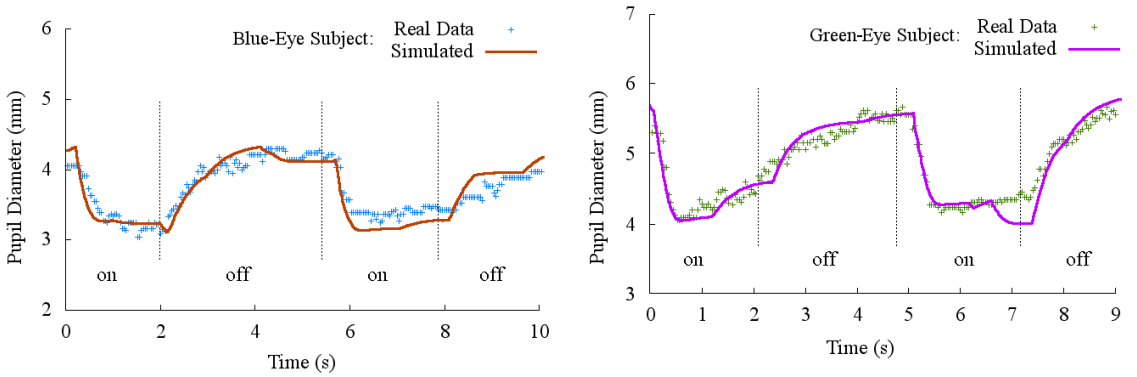

Figura B.4: Comparação entre os resultados simulados e medidas a partir de dados reais. O '+' verde e o 'x' azul representam, respectivamente, o diâmetro pupilar medido a partir de duas seqüências de vídeos: um com um indivíduo de íris verdes e outro de íris azuis. As linhas sólidas e tracejadas representam o diâmetro pupilar estimado pelo nosso modelo. As linhas verticais delimitam os intervalos de luz ligada e desligada. Note que a simulação aproxima muito bem os dados reais.

B.3 Modelo Para Deformação dos Padrões da Íris

O modelo para deformação dos padrões da íris, proposto neste trabalho, foi criado a partir de um conjunto de fotos capturadas durante um processo de dilatação pupilar induzido envolvendo cinco voluntários. As melhores fotos foram separadas, ordenadas pelo tamanho da pupila e as características mais salientes das íris foram marcadas manualmente. A Figura B.5 mostra um subconjunto dos pontos analisados. Note que os padrões movem-se radialmente e, desconsiderando as perturbações provocadas pelas estruturas das írises dos voluntários, o comportamento de cada saliência pode ser aproximado por uma linha reta. Além disso as saliências permanecem em suas posições relativas a largura da pupila, caracterizando uma invariância que define o nosso modelo.

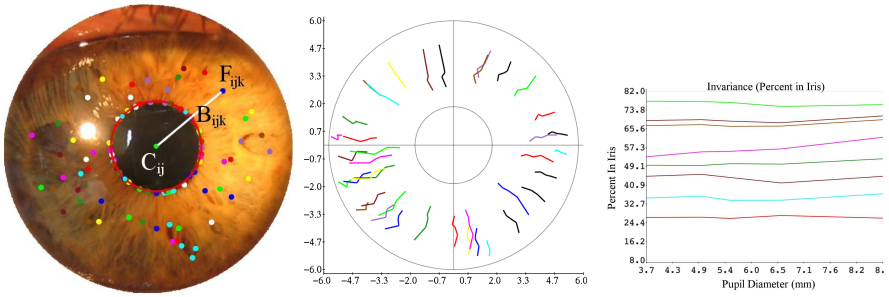

Figura B.5: Esquerda: Fotografia da íris de um voluntário durante o processo de dilatação. Os pontos coloridos indicam as saliências analisadas. Centro: Um gráfico mostrando o comportamento de cada ponto analisado durante a dilatação da pupila. Direita: Um gráfico que apresenta, em percentual, a posição de um subconjunto das saliências relativo a largura da íris. Observa-se que os pontos se movem ao longo de trajetórias aproximadamente radiais e mantêm suas posições relativamente à largura da íris.

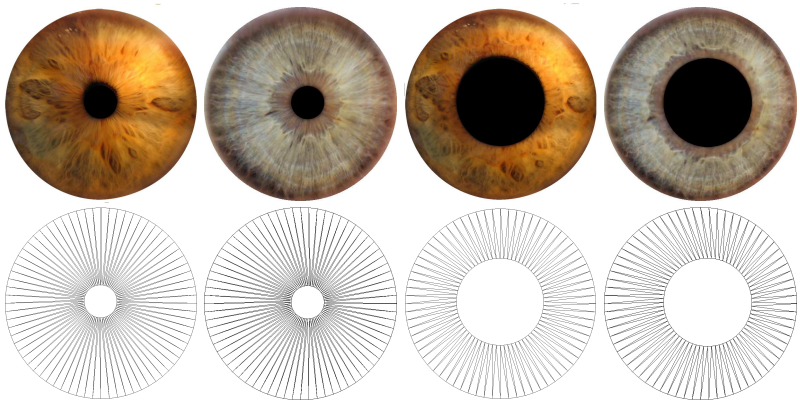

Figura B.6: Exemplos de íris renderizadas usando o modelo proposto. Cima: imagens geradas a partir de intensidades de luz de 10^5 Blondels (esquerda) e 1 Blondel (direita). Baixo: malhas de triangulos usadas para renderizar.

A animação da deformação dos padrões radiais é feita usando uma malha em *triangle-strip* sobre um disco definido por dois círculos que delimitam a íris (Figura B.6 baixo) e com uma fotografia de uma íris com uma pupila pequena como textura. As coordendas de textura da borda da pupila são mapeadas para o círculo interno, enquanto que as da borda externa da íris são mapeadas para o círculo mais externo. A animação modifica a posição dos pontos da borda interna, aumentando o diminuindo o raio do círculo que a define, sem

alterar as coordenadas de textura. Figura B.7 mostra resultados produzidos pelo modelo de deformação proposto, comparando-os com fotografias de iris reais.

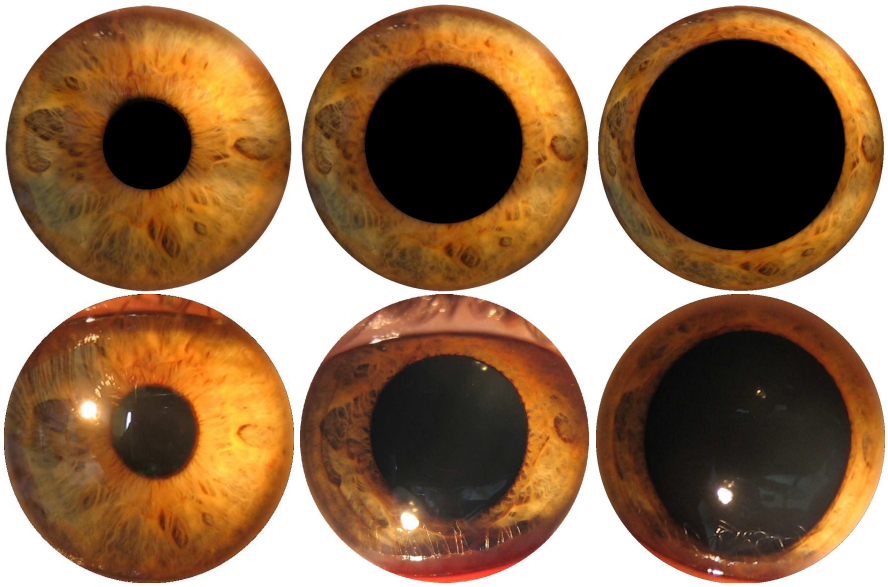

Figura B.7: Comparação dos resultados produzidos pelo modelo proposto com um conjunto de fotografias. Cima: imagens renderizadas usando o modelo de deformação de padrões para ambientes iluminados com $35.638,70$ e $2.928,78$ lumens/mm^2, respectivamente, para as duas primeiras imagens. A terceira simula uma indução por medicamento. Baixo: fotografias da íris humana com diferentes diâmetros pupilares.

B.4 Conclusões

Esta dissertação apresenta novos modelos para síntese realista do comportamento da íris e pupila humana. O modelo para reflexo pupilar à luz combina e estende resultados teóricos com dados experimentais coletados por vários pesquisadores. O modelo resultante é expressado em termos de uma equação diferencial com atraso que descreve as mudanças no diâmetro pupilar em função da iluminação ambiente. O modelo é original no sentido de simular as diferenças individuais e a hippus em função da iluminação. Os modelos foram validados através de comparações dos resultados simulados com fotografias e vídeos capturados de íris humanas. A qualidade da predição ultrapassou as nossas expectativas, dado o pequeno número de parâmetros envolvido.

O nosso modelo fisiológico é o primeiro a simular o PLR da literatura de computação gráfica. É o primeiro modelo prático na literatura para simular a dinâmica da pupila e íris em condições de iluminação não constantes e o primeiro modelo integrado em toda a literatura a considerar variabilidade individual usando equações gerais para latência, velocidade e hippus. Nosso modelo para deformação é também o primeiro modelo deste tipo na área de computação gráfica. Nossos resultados devem encontrar aplicabilidade imediata em diversas áreas que requerem animações faciais com alto detalhe, como em filmes de animação, onde a busca por cenas mais realistas nunca termina. Além disso, espera-se que os modelos propostos nessa dissertação impactem áreas como biologia e oftalmologia, onde eles podem ser utilizados, por exemplo, para simulações e diagnósticos de patologias.